Geochimica et Cosmochimica Acta 384 (2024) 27–43

Contents lists available at ScienceDirect

Geochimica et Cosmochimica Acta

journal homepage: www.elsevier.com/locate/gca

Thermodynamics and kinetics of cation partitioning between plagioclase and trachybasaltic melt in static and dynamic systems: A reassessment of the lattice strain and electrostatic energies of substitution

Silvio Mollo [a,b,*], Fabrizio Di Fiore [b], Alice MacDonald [c], Teresa Ubide [c], Alessio Pontesilli [b], Gabriele Giuliani [d], Alessandro Vona [d], Claudia Romano [d], Piergiorgio Scarlato [b]

[a] Department of Earth Sciences, Sapienza – University of Rome, P. le Aldo Moro 5, 00185 Roma, Italy
[b] National Institute of Geophysics and Volcanology, Section of Roma 1, Via di Vigna Murata 605, 00143 Roma, Italy
[c] School of the Environment, The University of Queensland, St Lucia, 4072 Brisbane, QLD, Australia
[d] Dipartimento di Scienze, University of Roma Tre, L.go San Leonardo Murialdo 1, 00146 Roma, Italy

ARTICLE INFO

Associate editor: Yuan Li

Keywords:
Plagioclase
Partition coefficients
Lattice strain and electrostatic energies
Compositional controls on cation partitioning

ABSTRACT

Most of the solidification history of magmas beneath active volcanoes takes place in chemically and physically perturbed plumbing systems where the growth of crystals is collectively governed by a range of kinetic processes related to the dynamics of crustal reservoirs and eruptive conduits. In this context, we have experimentally investigated the partitioning of major, minor, and trace cations between plagioclase and trachybasaltic melt under conventional static (no physical perturbation) and dynamic (melt stirring) crystallization regimes. Slow interface reaction kinetics are established between the advancing crystal surface and the adjacent melt, as the result of the combined control of a small degree of effective undercooling, prolonged diffusive relaxation, and convective homogenization. The kinetic aspects of plagioclase growth influence the partitioning of trace cations during transport of structural units across the crystal-melt interface, with consequent departure from macroscopic equilibrium in the system. The type and number of charge–balanced and –imbalanced configurations produced by the accommodation of trace cations into the coordination polyhedron can be thermodynamically rationalized in terms of lattice strain and electrostatic partitioning energetics. However, the overall solution energy accompanying trace cation kinetic substitutions cannot be entirely deconvoluted from major component activities in both melt and plagioclase phases. The emerging view that slow interface kinetic processes may lead to strong compositional dependence for the partition coefficient in dynamic subvolcanic environments contrasts markedly with the conventional idea that the energetics of cation partitioning are dominantly controlled by the effect of isothermal changes in the bulk system.

1. Introduction

In the ideal formula of plagioclase (MT_4O_8), cations are ordered in both tetrahedral (T) and octahedral (M) sites forming two characteristic end-members for anorthite ($CaAl_2Si_2O_8$; An^{pl}) and albite ($NaAlSi_3O_8$; Ab^{pl}). For a system in a thermodynamically stable state, the albite-anorthite exchange can be parameterized according to the free energy of fusion (ΔG_{fusion}) of the equilibrium reactions $Ab^{pl} = Ab^{melt}$ and $An^{pl} = An^{melt}$, expressed as the difference between the Gibbs free energy of plagioclase and melt of the same composition at constant temperature (Putirka, 2017). This thermodynamic formulation defines a compositional domain within which the stochiometric solution of fictive trace element components at infinite dilution in plagioclase is an explicit provision for the Nernst partition coefficient $D_i = C_i^{pl}/C_i^{melt}$, where C_i is the concentration of the trace cation i of interest (Blundy and Wood, 1991; Kneip and Liebau, 1994; Peters et al., 1995; Bindeman and Davis, 2000; Dohmen and Blundy, 2014; Sun et al., 2017; Schoneveld and O'Neill, 2019). At very high dilution of trace cations, the entropic effects of dissociation of the charge-balancing major cations in the coordination polyhedron likely overwhelm the energy of association (Wood and Blundy, 2001). In that respect, the partitioning energetics associated with heterovalent substitutions are subordinate to an excess free energy

* Corresponding author at: Department of Earth Sciences, Sapienza – University of Rome, P. le Aldo Moro 5, 00185 Roma, Italy.
E-mail address: silvio.mollo@uniroma1.it (S. Mollo).

https://doi.org/10.1016/j.gca.2024.09.006
Received 15 May 2024; Accepted 3 September 2024
Available online 10 September 2024

change ($\Delta G_{partitioning}$) gained by the accommodation of a trace cation with ionic radius and charge different from those of the major cation originally hosted in the crystallographic site of plagioclase. Of particular importance is that $\Delta G_{partitioning}$ encapsulates two energetic terms that comparatively describe large enthalpic effects for the free energy of substitution: 1) distortion of the lattice (ΔG_{strain}) due to ionic radius mismatch and 2) changes in the electrostatic forces ($\Delta G_{electrostatic}$) due to charge mismatch (Blundy and Wood, 1994, 2003a, 2003b; Wood and Blundy, 2001, 2003).

Beyond the domain of classical thermodynamics, several kinetic processes prompt the growth of plagioclase in natural magmatic environments upon the effect of variable degrees of undercooling ($\Delta T = T_{liquidus} - T_{crystallization}$), induced by either a decrease in temperature or the increase of H_2O exsolution during magma decompression (Mollo and Hammer, 2017). An explicit manifestation of ΔT is the development of supersaturated melts resulting from imbalance between the rate at which the crystal surface advances and the rate of cation diffusion in the melt (Lasaga, 1998). After an initial degree of ΔT, however, the crystal growth rate progressively declines over time, causing the concentration gradients in the melt adjacent to the crystal surface to decrease by diffusive relaxation (Mollo and Hammer, 2017). A side effect of interface reaction kinetics on plagioclase is the development of crystals enriched in An^{pl} and mutually depleted in Ab^{pl} compared to systems at the thermodynamic equilibrium (Mollo et al., 2012; Vetere et al., 2015; Humphreys et al., 2016), with consequent modification of the of the *liquidus-solidus* binary loop topology (Iezzi et al., 2014) and substantial variation in the magnitude of D_i (Mollo et al., 2011).

Volcanic settings represent physically and chemically perturbed systems in which convective mass transfer is associated with the upward migration of magma across multiple interconnected crustal reservoirs and during eruption towards the surface (Worster et al., 1990; Forni et al., 2018; Ubide and Kamber, 2018; Di Stefano et al., 2020). The net effect of turbulence is to disperse chaotically the suspended crystals over a broad range of convective velocities and flow regimes (Marsh, 1988; Huppert and Sparks, 1980; Di Fiore et al., 2022). Under such circumstances, crystal growth is influenced by complex kinetic and dynamic reactions, especially at shallow crustal pressures and along volcanic conduits (Lanzafame et al., 2017). Despite their unquestionable importance and merit, existing partitioning data and models derived for static and unperturbed systems cannot unequivocally address the complexity of natural subvolcanic environments, for which the phenomenological treatment of reaction kinetics plays a pivotal role in the compositional evolution of energetically unstable magmatic systems (cf. Mollo et al., 2023). To date, little is known about the effect of dynamic crystallization on cation partitioning, but there exists circumstantial evidence for its leverage on the solidification history of magmas at pre- and syn-eruptive conditions (Watson and Müller, 2009; Di Fiore et al., 2021a).

According to the above considerations, the purpose of the present study is to examine at the laboratory scale how slow interface reaction kinetics between the advancing surface of plagioclase and a trachybasaltic melt are cooperatively governed by transport and relaxation phenomena arising from a small degree of undercooling and the homogenizing control of convective stirring. Our experimental approach indicates that the partitioning energetics of trace cations are primarily controlled by the kinetic aspects of plagioclase growth in a non-equilibrium bulk system. During transport of structural units across the crystal-melt interface, the magnitude of D_i can be rigorously described by the expression $\Delta G_{partitioning} = \Delta G_{strain} + \Delta G_{electrostatic}$. From a thermodynamic standpoint, major component activity models derived for melt and plagioclase compositions may effectively illustrate the energy change associated with kinetic incorporation of trace cations in the lattice site. We conclude that the textural attributes of plagioclase, the mixing properties of solid solution components and, ultimately, the partitioning energetics of trace cation substitutions are collectively influenced by the shift from static to dynamic crystallization regimes, provided that the crystal growth proceeds isothermally over the time scale of crystallization.

2. Material and methods

2.1. Starting material and experiments

The starting material used in this study is a trachybasaltic scoria from the 2002–2003 eruptive sequence at Mt. Etna volcano (Supplementary Material). To achieve trace element contents analyzable with a high precision, the powdered natural juvenile material was doped with additional oxides representative of the most important geochemical groups for rare earth elements (0.1 wt% REE), high field strength elements (0.1 wt% HFSE), large ion lithophile elements (0.1 wt% LILE) and transition elements (0.1 wt% TE). Obeyance of Henry's Law was guaranteed using a low doping level for total trace element oxides, not exceeding 0.4 wt%. Then the doped material was loaded in a Fe-presaturated Pt-crucible and melted at 1,300 °C in a Nabertherm $MoSi_2$ atmospheric pressure chamber furnace installed at the EVPLab of the University of Roma Tre. The oxygen fugacity within the chamber furnace was self-buffered to that of air ($\log fO_2 = -0.68$), in conformity to the redox state condition imposed by the concentric cylinder apparatus (see below). After a dwell time of 5 h, the nominally anhydrous melt was quenched to a glass in air. The glass was analyzed by X-ray powder diffraction and scanning electron microscopy, and no crystalline phases were detected.

Plagioclase crystallization experiments (Table 1) were carried out in a concentric cylinder apparatus consisting of a Theta Industries Rheotronic II Rotational Viscometer equipped with 1) an Anton Paar Rheolab Qc rotational rheometer (torque full-scale of 75 mNm), 2) a factory calibrated S-type thermocouple (accuracy of ±2 °C), and 3) Fe-presaturated $Pt_{80}Rh_{20}$ crucible and spindle (see Di Fiore et al., 2022 for further details). To ensure early melt relaxation, a $T_{superliquidus}$ pretreatment was applied by melting the glassy starting material at 1,300 °C (heating rate of 25 °C/min) for 1 h. All the experiments were conducted under atmospheric pressure and air redox state. No gas mixtures were used to reduce fO_2, owing to technical limitations of the experimental set-up (Di Fiore et al., 2021b). While the air redox condition does not directly influence natural magmatic processes, conducting partitioning experiments with cations in high valence states presents an opportunity to deepen our understanding of how these cations are incorporated into the lattice site of plagioclase. This is particularly relevant when studying redox-sensitive and aliovalent substitutions that necessitate charge balance (Bindeman et al., 1998; Bindeman and Davis, 2000; Miller et al., 2006; Dohmen and Blundy, 2014). At the end of each experiment, the sample was quenched at ~120 °C/min by holding the crucible walls under flowing water. The effect of melt supersaturation on crystallization was isolated by conducting a set of conventional static undercooling (*SU*) experiments with no physical perturbation, in which the spindle was placed outside the crucible and a certain degree of undercooling was imposed in absence of stirring. On the other hand, a set of dynamic undercooling (*DU*) experiments was designed to investigate the combined effects of melt supersaturation and convection in physically dynamic systems. After $T_{superliquidus}$ pretreatment, the melt was cooled in both *SU* and *DU* to the target temperature (T_{target}) at a rate of 25 °C/min. T_{target} was 1185 °C and 1170 °C for *SU*, whereas T_{target} was 1170 °C for *DU*. The temperature was held constant for an annealing time (t_{ann}) of 72 h to ensure melt relaxation and minimization of chemical concentration gradients imposed by the initial effect of undercooling (cf. Pontesilli et al., 2019; Mollo et al., 2020). The shear rate ($\dot{\gamma}$) used for *DU* was 0.1, 1, and 10 s^{-1}. According to the experimental range of $\dot{\gamma}$ and *T*, *SU* products are hereinafter referred to as *SU-1185* and *SU-1170*, whereas *DU* products are hereinafter referred to as *DU-1170–0.1*, *DU-1170–1*, and *DU-1170–10*. A further static (*ST*) experiment was conducted with a Pt-loop suspended within the furnace (Table 1). For this nominally equilibrium experiment, the oxygen fugacity was buffered to the air redox state, in accord with *SU* and *DU* conditions. The experimental

Table 1
Crystallization experiments carried out under static and dynamic conditions. Phase relations and plagioclase textural attributes are also reported in table. Acronyms refer to: *pl*, plagioclase, timt, titanomagnetite; *gl*, glass; *P*, pressure; *T*, temperature; fO_2, oxygen fugacity; $\dot{\gamma}$, shear rate; t_{ann}, annealing time; *CR*, cooling rate; V_{pl}, volumetric proportion of pl; n^o, nucleation density of *pl*; L_d, characteristic length of *pl*; N_V, number of *pl* crystals per unit volume; τ, crystallization time; *G* and *J*, growth and nucleation rate of *pl*, *respectively*. CSD_{slope} and $CSD_{intercept}$, data from crystal size distribution (*CSD*) analysis of *pl*.

Run	$T_{superliquidus}$ (°C)	*CR* (°C/min)	T_{target} (°C)	t_{ann} (h)	$\dot{\gamma}$ (s^{-1})	*P* (bar)	$\log fO_2$ (buffer)	Phase assemblage	CSD_{slope} (mm^{-1})	$CSD_{intercept}$ (mm^{-4})	V_{pl} (%)	$\ln(n^o)$ (mm^{-4})	$\ln(N_v)$ (mm^{-3})	L_d (mm)	$\ln(G\tau)$ (mm)	$G\times10^6$ (mm s^{-1})	$J\times10^{-3}$ (mm^{-3} s^{-1})
SU-1185	1300	25	1,185	72	–	1	air	timt, gl	–	–	–	–	–	–	–	–	–
SU-1170	1300	25	1,170	72	–	1	air	timt, pl, gl	−2.53	5.86	10	5.86	4.75	0.40	−0.93	1.52	0.54
DU-1170–0.1	1300	25	1,170	72	0.1	1	air	timt, pl, gl	−3.43	8.08	11	8.08	4.84	0.29	−1.23	1.12	3.64
DU-1170–1	1300	25	1,170	72	1	1	air	timt, pl, gl	−4.39	9.07	13	9.07	5.26	0.23	−1.48	0.88	7.66
DU-1170–10	1300	25	1,170	72	10	1	air	timt, pl, gl	−8.14	10.54	14	10.54	6.06	0.12	−2.10	0.47	17.96
ST-1170	–	–	1,170	72	–	1	air	timt, pl, gl	−10.94	11.06	14	11.06	6.04	0.09	−2.39	0.35	22.55

charge was heated at a rate of 25 °C/min from room temperature directly to T_{target} of 1,170 °C, thus precluding any physicochemical effect due to 1) melt supersaturation via $T_{superliquidus}$ pretreatment and 2) melt convection due to continuous stirring. The temperature was kept constant for t_{ann} of 72 h before quench and the resulting experimental product is hereinafter referred to as *ST-1170*. All the run products from *SU-1185–1170*, *DU-1170–0.1–1-10*, and *ST-1170* were mounted in epoxy and polished thin sections were produced from the epoxy disks.

2.2. Image acquisition, segmentation, and crystal size distribution analysis

Photomicrographs of the experimental samples were collected in the backscattered electron (BSE) mode of a JEOL 6500F field emission gun scanning electron microscopy (FE-SEM) equipped with an energy-dispersive spectrometer (EDS) detector and installed at the HP-HT Laboratory of Experimental Volcanology and Geophysics of the Istituto Nazionale di Geofisica e Vulcanologia (INGV), Rome, Italy.

BSE photomicrographs were processed using *NIH ImageJ* software and reduced to binary (black and white) images by grey level thresholding. This image segmentation required the selection of the upper and lower thresholds for a gray-scale image. The best tones of grey associated with plagioclase were determined by improving recognition of an individual known crystal via image manipulation (i.e., smoothing, sharpening, and trimming), following the same approach described in Higgins (2006). Segmented crystal fragments at the edge of images were considered as artefacts and removed from the data set. The uncertainty associated with the segmentation process was evaluated by adding/subtracting pixel layers around each crystal in the binarized image (cf. Pontesilli et al., 2019; Moschini et al., 2021).

CSDCorrections 1.38 (Higgins, 2000) was employed to perform crystal size distribution (*CSD*) analysis and determine binned curves sorted in different plagioclase crystal size classes. Planar data of crystal intersections were converted into volume data by applying stereological correction for cut-section effects and intersection probability effects. Plagioclase aspect ratios for *short:intermediate:long* crystal axes (in mm) were calculated with *CSDslice* (Morgan and Jerram, 2006), by comparing 2D raw data with a crystal habit data set and determining the five best matching 3D crystal shapes. All these measurements can be found in the Supplementary Material.

According to the pioneer works of Marsh (1988) and Cashman (1990), all *CSD* data were treated in the form of semi-logarithmic *L* against ln(*n*) plots:

$$\ln(n) = \ln(n^o) - \frac{L}{G\tau} \quad (1)$$

where *n* is the number of plagioclase crystals per unit length per unit volume (in mm^{-4}), according to the density distribution of crystals with length *L* (in mm) per unit volume per bin size. The number density of nuclei-sized crystals n° (or nucleation density in mm^{-4}) corresponds to the intercept of the *CSD* curve at $L = 0$ and represents the number of plagioclase crystals of zero size in Eq. (1). The slope of the *CSD* curve is $-1/G\tau$, where *G* is the crystal growth rate (in mm s^{-1}) and τ is the crystal growth time (in seconds). The crystal nucleation rate *J* is related to the growth rate by the formula $J{=}n^oG$. The dominant size of plagioclase L_d (or characteristic length in mm) is inversely proportional to the slope of the *CSD* curve as $L_d = -1/CSD_{slope}$. The volumetric proportion of plagioclase V_{pl} is expressed in percentage, whereas the number of crystals per unit volume (in mm^{-3}) is calculated as $N_V = L_dCSD_{intercept}$ (Marsh, 1988; Cashman, 1990). All these textural parameters determined for plagioclase crystal populations are reported in Table 1.

2.3. Major, minor, and trace element analyses

Major and minor oxide concentrations of plagioclase crystals and

glasses were obtained on polished and carbon-coated epoxy disks at the HP-HT Lab of INGV using a JEOL-JXA8200 electron probe microanalyzer (EPMA) equipped with five wavelength dispersive spectrometers. All these analyses can be found in the Supplementary Material, also in comparison with the glassy starting material and the original bulk rock. An accelerating potential of 15 kV was employed for the analysis of glasses. The beam current was tuned at 20 nA and defocused to a 10 μm spot size. Counting times were 20 s on-peak and 10 s for background, except for Na and K (10 s peak/5 s background) that were analyzed first to minimize alkali migration. Matrix correction was undertaken using a ZAF (Z: atomic number; A: absorption; F: fluorescence) procedure. Plagioclase crystals were analyzed using a 20 kV and 15 nA beam with 10 μm spot size. Counting times were the same as those adopted for the glass analysis. Following Miller et al. (2006), Fe, Mg, and Ti were acquired at 15 kV and 400 nA with a focused beam of 5 μm diameter, for 90 s on-peak and 45 s per background, to improve the counting statistics. Calibration standards were albite (Si-PET, Al-TAP, Na-TAP), forsterite (Mg-TAP), augite (Fe-LIF), apatite (Ca-PET, P-PET), orthoclase (K-PET), rutile (Ti-PET), and rhodonite (Mn-LIF). MAC augite and albite were used as a quality monitors. Accuracy and precision from secondary standards were typically better than 1–3% for elements with abundance >1 wt%. For elements with abundance < 1 wt%, accuracy was typically better than 1–5%. Analytical precision determined using the EPMA outputted uncertainty based on counting statistics for each analysis was better than 1% and 7% for elements with abundances >10 wt% and <10 wt%, respectively. For mapping, we used an accelerating voltage of 20 kV and a current of 200nA, with 2 μm/pixel resolution and 200 ms acquisition time per pixel, measuring up to 5 elements per analysis (one per diffracting crystal).

Trace element concentrations of plagioclase crystals and glasses were determined with laser ablation inductively coupled plasma mass spectrometry (LA-ICP-MS) at The University of Queensland Centre for Geoanalytical Mass Spectrometry, Radiogenic Isotope Facility (UQ RIF-lab). All these analyses can be found in the Supplementary Material. We used an ASI RESOlution 193 nm excimer UV ArF laser ablation system with a dual-volume Laurin Technic ablation cell and GeoStar Norris software, coupled to a Thermo iCap RQ quadrupole mass spectrometer with Qtegra software. Ablation was performed in ultrapure He to which Ar make-up gas with a trace amount of N_2 was added for efficient transport and to aid ionization. Analyses were conducted using a spot size of 30 μm, repetition rate of 10 Hz, and on-sample fluence of 3.5 J/cm^2 for 40 s, with 20 s background measurement between spots. Data reduction was carried out using Iolite v.4 (Paton et al., 2011) in quantitative mode. The NIST612 glass reference material was the calibration standard employed for all analyzed elements, and Si concentrations measured via electron microprobe on plagioclase and glass were employed as internal standards. BCR-2G, BHVO-2G, and NIST610 glass reference materials were used as secondary standards to monitor accuracy and precision. For all analytical sessions, precision was typically better than 5% and accuracy was better than 15% (Supplementary Material).

3. Results

3.1. Phase assemblage and plagioclase morphology

The experimental phase assemblage consists of titanomagnetite, plagioclase, and residual glass (Fig. 1). Looking at the high-temperature experiment *SU-1185*, titanomagnetite is the first phase to appear on the *liquidus*, mainly in response to the air redox state of the melt. Plagioclase cosaturates the melt in the low-temperature experiment *SU-1170* (Table 1). Under static undercooling conditions, the volumetric proportion of plagioclase is 10%, whereas it increases up to 14% with increasing stirring under dynamic undercooling conditions. The volumetric proportion of titanomagnetite is typically less than 5% in all the experiments.

By comparing the phase assemblages from *SU-1185* and *SU-1170*, it is apparent that the crystallization of plagioclase occurs within a restricted thermal interval that corresponds to a small degree of effective undercooling ($\Delta T_{eff} \leq 15$ °C). ΔT_{eff} is the difference between the phase-in and system temperatures, as an estimate of the actual supersaturation still imposed to the melt after some crystallization of titanomagnetite has taken place. This driving force for crystallization promotes the growth of large and elongate plagioclase crystals in *SU-1170*, showing polyhedral, tabular, and hopper morphologies (Fig. 1).

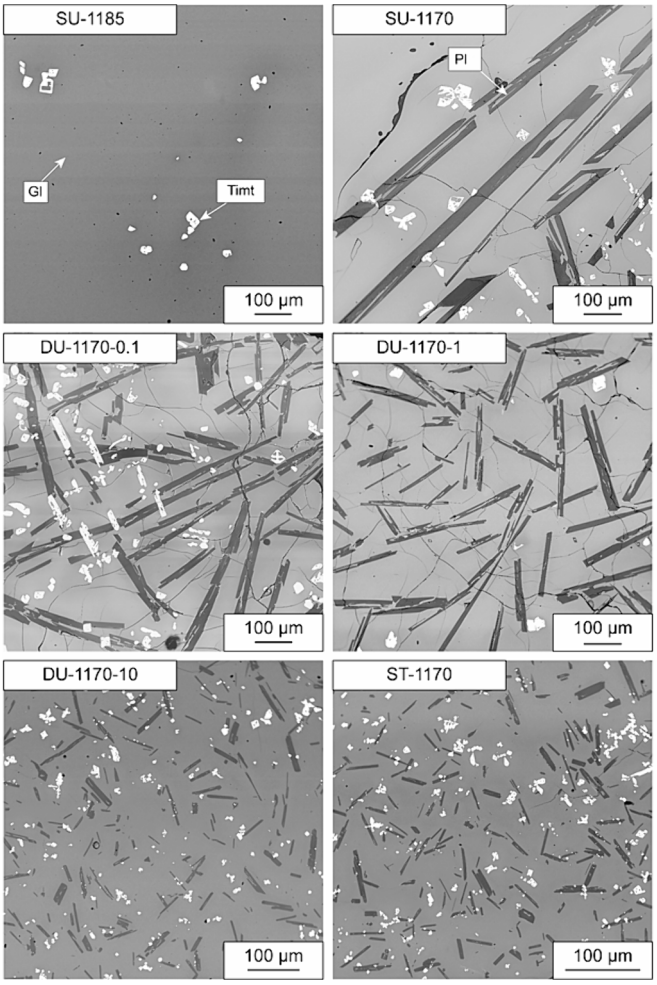

Fig. 1. Representative backscattered electron photomicrographs of static and dynamic crystallization experiments. Gl, glass. Pl, plagioclase. Timt, titanomagnetite.

In dynamic undercooling experiments, as shear rate increases from *DU-1170–0.1* to *DU-1170–1* to *DU-1170–10* ($\dot{\gamma}$ = 0.1, 1 and 10 s^{-1}, respectively), plagioclase crystals with well-defined polyhedral forms and smaller sizes develop from the stirred melt (Fig. 1). Small-sized crystals are also found in *ST-1170* and their textural features are very similar to those observed in *DU-1170–10* (Fig. 1).

3.2. Crystal size distribution (CSD) analysis

Plagioclase *CSD* curves for all the experiments are characterized by well-defined steep linear trends (R^2 = 0.94–1.00, where R is the coefficient of determination), with weak concave-up shapes due to a continuous gradient from larger to smaller crystal sizes (Fig. 2a). Irrespective of the experimental approach adopted, plagioclase populations are delineated by an increase of ln(n) and concurrent decrease of L, leading to CSD_{slope} and $CSD_{intercept}$ varying from −2.53 to −10.94 and from 5.87 to 11.06, respectively (Fig. 2a and Table 1). The tight linear correlation (R^2 = 0.92) between ln($G\tau$) and ln(n^O) (Fig. 2b) indicates

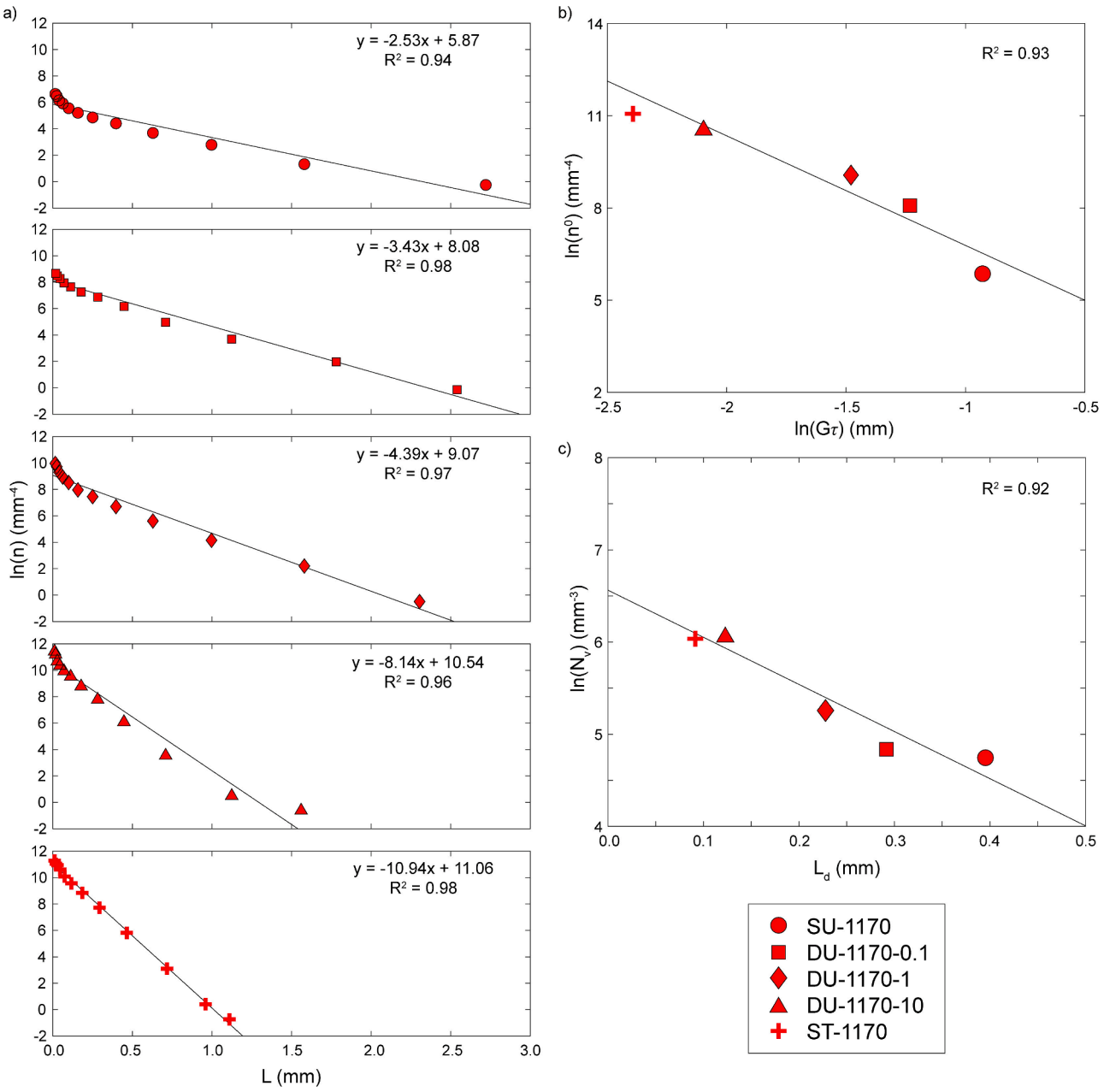

Fig. 2. Crystal size distribution curves of plagioclase from static and dynamic crystallization experiments, in semi-logarithmic plots of crystal length L against the number of crystals per unit length per unit volume ln(n) (a). Plot of the crystal growth rate multiplied by the crystallization time ln($G\tau$) against the crystal nucleation density ln(n^O) (b). Plot of the crystal characteristic length L_d against the number of crystals per unit volume ln(N_v) (c).

that the nucleation density, growth rate, and growth time are all function of crystallization kinetics, following the theoretical relationship that $n^o = J/G$, in accord with the concurrent decrease of both J and G with τ (Cashman, 1990; Blundy and Cashman, 2008). The textural parameter ln($G\tau$) reaches its maximum value for the largest-sized crystals in *SU-1170*. As $\dot{\gamma}$ increases, the magnitude of ln($G\tau$) decreases approaching the lowest value determined for the smallest-sized crystals in *ST-1170* (Fig. 2b and Table 1). Comparing *ST-1170* and *SU-1170*, it becomes evident that the effect of ΔT_{eff} in *SU-1170* strongly favors the growth rate of plagioclase by limiting its nucleation rate (i.e., highest G and lowest n^o in Fig. 2b). Conversely, in *ST-1170*, the absence of melt supersaturation causes the nucleation rate to prevail over the growth rate (i.e., lowest G and highest n^o in Fig. 2b). The primary effect of stirring on melt crystallization is to reduce the activation energy of nucleation by enhancing the mobility of atoms and increasing their probability of random collisions in the melt phase, leading to the germination of plagioclase crystal nuclei (i.e., Di Fiore et al., 2023, 2024). Consequently, G decreases and n^o concurrently increases as $\dot{\gamma}$ increases from 0.1 to 10 s^{-1}, placing *DU-1170–0.1–1-10* in between *ST-1170* and *SU-1170*, and resulting in intermediate values for G and n^o (Fig. 2b).

The statistically significant linear fit ($R^2 = 0.92$) between L_d and ln(N_v) confirms that the characteristic length of plagioclase gradually decreases from *SU-1170* (0.40 mm) to *DU-1170–0.1–1-10* (0.29–0.12 mm) to *ST-1170* (0.09 mm), as the number of crystals per unit volume concurrently increases from 115 to 426 mm^{-3} (Fig. 2b and Table 1). Highest values of L_d for *SU-1170* are primarily attributed to the influence of ΔT_{eff} in governing the formation of large plagioclase crystals (Fig. 2b, c). Conversely, lowest values of L_d for *ST-1170* indicate rapid minimization of the interfacial free energy between small crystals and the

surrounding melt in the nominally equilibrium experiment, in consideration of the fact that no *superliquidus* pretreatment or undercooling were imposed to the experimental charge. In *DU-1170–0.1–1-10*, kinetic effects at the interface melt are suddenly mitigated by vigorous convective mass transfer, and values of L_d progressively decrease with increasing stirring (Fig. 2b, c). Therefore, absence of a *superliquidus* pretreatment and/or application of a dynamic physical perturbation are two conditions that inhibit the role of undercooling as driving force for the crystal growth, causing little free energy difference at the crystal-melt interface and consequent decrease of the crystal size.

3.3. Plagioclase growth rate

The time scale of cooling from $T_{superliquidus}$ to T_{target} (~5 min) is much shorter than the annealing treatment of 72 h at which the textural evolution of plagioclase proceeds isothermally. Therefore, t_{ann} can be combined with CSD_{slope} to estimate the crystal growth rate, as frequently adopted in the literature (see for example the review study of Moschini et al., 2023). The magnitude of G is observed to decrease on the order of 1.5×10^{-6} (*SU-1170*), 1.1×10^{-6} (*DU-1170–0.1*), 8.8×10^{-7} (*DU-1170–1*), 4.7×10^{-7} (*DU-1170–10*), and 3.5×10^{-7} mm s^{-1} (*ST-1170*) (Table 1). This conservative range of values corresponds to that of 10^{-6}-10^{-7} mm s^{-1} experimentally derived for plagioclase crystals grown upon small ΔT_{eff}, ranging from 11 to 30 °C (Moschini et al., 2023).

3.4. Ca-Na exchange between plagioclase and melt

Within the analytical resolution of 2 μm pixel size, microprobe chemical maps of Al_2O_3, CaO, and Na_2O document the growth of unzoned plagioclase crystals surrounded by a chemically homogeneous glass composition in both static (Fig. 3a) and dynamic (Fig. 3b) experiments.

Fig. 4a shows that the average mole fraction of anorthite (X^{pl}_{An}; Supplementary Material) in plagioclase varies with the magnitude of ln ($G\tau$). A well-defined linear fit ($R^2 = 0.93$) is bracketed by two end-member compositions corresponding to *SU-1170* ($X^{pl}_{An} = 0.83$) and *ST-1170* ($X^{pl}_{An} = 0.76$). Intermediate compositions are measured for *DU-1170–0.1–1-10*, in which X^{pl}_{An} decreases from 0.81 to 0.77 as $\dot{\gamma}$ increases from 0.1 to 10 s^{-1}. It is worth stressing that changes in the Ab^{pl}-An^{pl} solid solution components cannot be due to different crystallization temperatures of the system (because T_{target} is always 1,170 °C), neither to the effect of H_2O dissolved in the melt on the *liquidus* depression of feldspar (as the experiments are nominally anhydrous). Therefore, any variation of X^{pl}_{An} closely depends on the role played by interface kinetics throughout the plagioclase growth process described by the textural attribute ln($G\tau$). Once atoms per formula unit (apfu) are calculated on the basis of 5 cations per 8 oxygens, the overall plagioclase composition is found to be always stochiometric (i.e., the sum of cations is 4.994–5.006 apfu; Supplementary Material). From plagioclase core to rim and along both short and long axes of plagioclase, X^{pl}_{An} shows very low standard deviations (1-σ = 0.002–0.004; Supplementary Material), in agreement with the formation of near-homogeneous crystalline layers upon the effect of sluggish interface kinetics (i.e., $\Delta T_{eff} \leq 15$ °C) and a prolonged annealing treatment (i.e., $t_{ann} = 72$ h).

Compared to the starting melt composition, residual trachybasaltic glasses are more enriched in SiO_2 (~49.0–50.2 wt%) and K_2O (~2.2–3.5 wt%) (Supplementary Material). The amount of MgO in the residual glass also increases (~5.2–6.7 wt%) due to the lack of mafic minerals in the phase assemblage of atmospheric pressure experiments. Conversely, the amount of all other major oxides is lower than that of the starting melt in response to titanomagnetite and plagioclase cosaturation. As the volumetric proportion of plagioclase increases relative to titanomagnetite with increasing stirring, the Fe_2O_3 content of the residual trachybasaltic glass is slightly higher in dynamic experiments

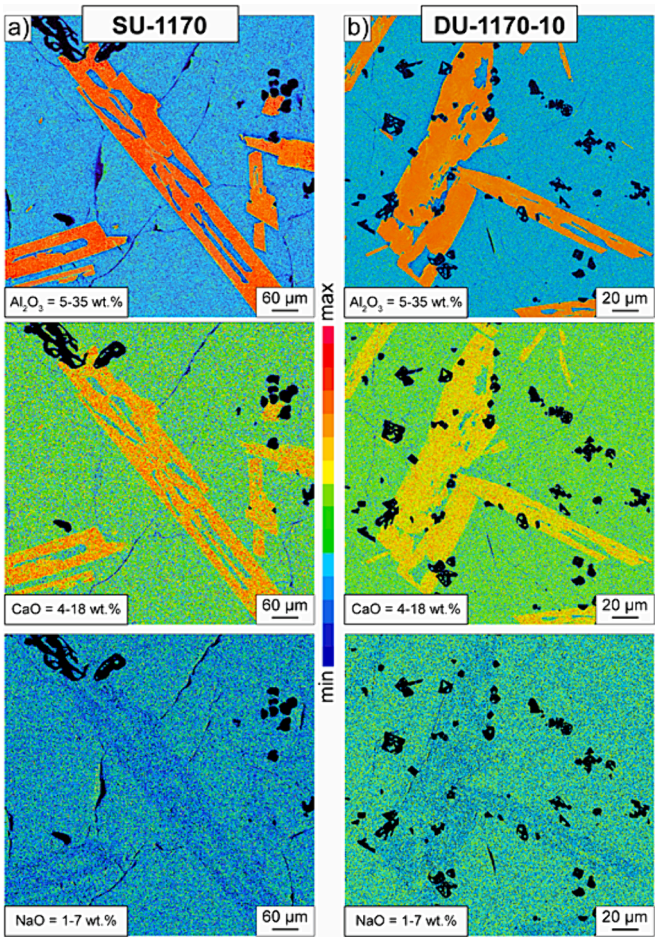

Fig. 3. Microprobe chemical maps of Al_2O_3, CaO, and Na_2O obtained for static *SU-1170* (a) and dynamic *DU-1170–10* (b) crystallization experiments.

(~8.4–8.6 wt%) compared to static experiments (~7.9–8.1 wt%). Chemical transects performed with a step size of 10 μm, starting from the crystal surface to a distance of ~100 μm into the melt, suggest that the residual glass is almost homogeneous within the microprobe analytical accuracy. Due to the low viscosity of mafic melts at high thermal regimes, the annealing treatment was likely enough long to minimize chemical concentration gradients in the melt, especially in consideration of the slow-diffusing chemical species (i.e., 1-σ_{SiO2} = 0.24–0.33 wt% and 1-σ_{Al2O3} = 0.07–0.12 wt%; Supplementary Material). However, it is also possible that plagioclase crystals continued to grow at the time of quenching. If that was the case, a very thin concentration boundary layer, which may not have been detectable within the resolution limit of microprobe analysis, could have been preserved at the crystal-melt interface.

The Ca-Na exchange partition coefficient [$Kd_{Ca-Na} = X^{pl}_{Ca}X^{melt}_{Na}/X^{pl}_{Na}X^{melt}_{Ca}$] is calculated for each experiment and subsequently compared with values obtained through the application of partitioning models from literature (Bindeman et al., 1998; Putirka, 2005; Dohmen and Blundy, 2014; Sun et al., 2017; Moschini et al., 2023). Fig. 4b illustrates that Kd_{Ca-Na} values from this study span 2.06 to 2.93, which is a relatively large variation range for experiments conducted isothermally with an identical starting melt composition. The Kd_{Ca-Na} calculated for the equilibrium experiment *ST-1170*, which underwent neither *superliquidus* pretreatment nor undercooling, aligns closely with the equilibrium line depicted by the model of Putirka (2005). In contrast, Kd_{Ca-Na} values calculated for both static undercooling (*SU-1170*) and dynamic undercooling (*DU-1170–0.1–1-10*) experiments deviate from the equilibrium model. The departure is more pronounced for *SU-1170*

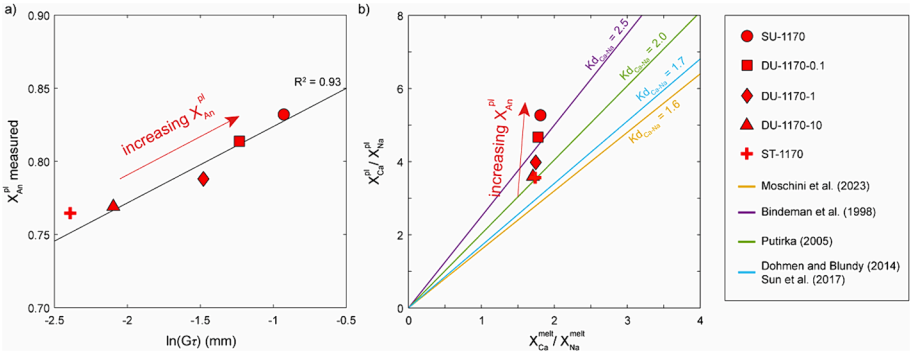

Fig. 4. Diagram showing the textural attribute of plagioclase ln($G\tau$) plotted against X_{An}^{pl} as a function of static and dynamic crystallization conditions (a). Plot of X_{An}^{pl} predicted using the equilibrium model of Moschini et al. (2023) against X_{An}^{pl} measured for experimental plagioclase crystals (b). Comparison between values of $Kd_{Ca\text{-}Na}$ from this study and those modeled using the equations of Bindeman et al. (1998), Putirka (2005), Dohmen and Blundy (2014), Sun et al., (2017), and Moschini et al. (2023) (c).

due to growth kinetics primarily governed by melt undercooling, whereas it is less significant for *DU-1170–10*, where the melt is more vigorously homogenized in response to the higher stirring rate applied.

3.5. Trace element partitioning

All major, minor, and trace partition coefficients calculated in this study are listed in the Supplementary Material, together with uncertainties (σ_D) derived by propagation of analytical errors on plagioclase and melt concentrations: $\sigma_D = [(\sigma_C^{pl}/C^{pl})^2 + (\sigma_C^{melt}/C^{melt})^2]^{0.5}$. Values of D_i are grouped according to the crystallographic site of plagioclase (M- or T-site), the cation valence ($^{M}i^{1+}$, $^{M}i^{2+}$, $^{M}i^{3+}$, and $^{M}i^{4+}$ for M−site, and $^{T}i^{3+}$ and $^{T}i^{4+}$ for the T-site), and the ionic radius (r_i). The coordination number of cations hosted in the M−site of plagioclase varies from six-to nine-fold due to large variations in the <M−O> bond distance (Kempster et al., 1962; Ribbe, 1983). Here we assume an eight-fold coordination and use ionic radii from Shannon (1976), in accordance with partitioning models from literature (e.g., Dohmen and Blundy, 2014; Sun et al., 2017; Bédard, 2023). Trace cations of interest for the M−site are: 1) monovalent Li, Rb, and Cs ($^{M}i^{1+}$) for $^{M}D_i^{+1}$, 2) divalent Zn, Sr, and Ba ($^{M}i^{2+}$) for $^{M}D_i^{+2}$, 3) trivalent rare earth elements (REE; from La to Lu) together with Y ($^{M}i^{3+}$) for $^{M}D_i^{+3}$, and 4) tetravalent high field strength elements (HFSE; Hf and Zr) together with actinides (U and Th) ($^{M}i^{4+}$) for $^{M}D_i^{+4}$. On the other hand, trace cations of interest for the T-site are: 1) trivalent Sc and Ga ($^{T}i^{3+}$) for $^{T}D_i^{+3}$, and 2) tetravalent Ge ($^{T}i^{4+}$) for $^{T}D_i^{+4}$.

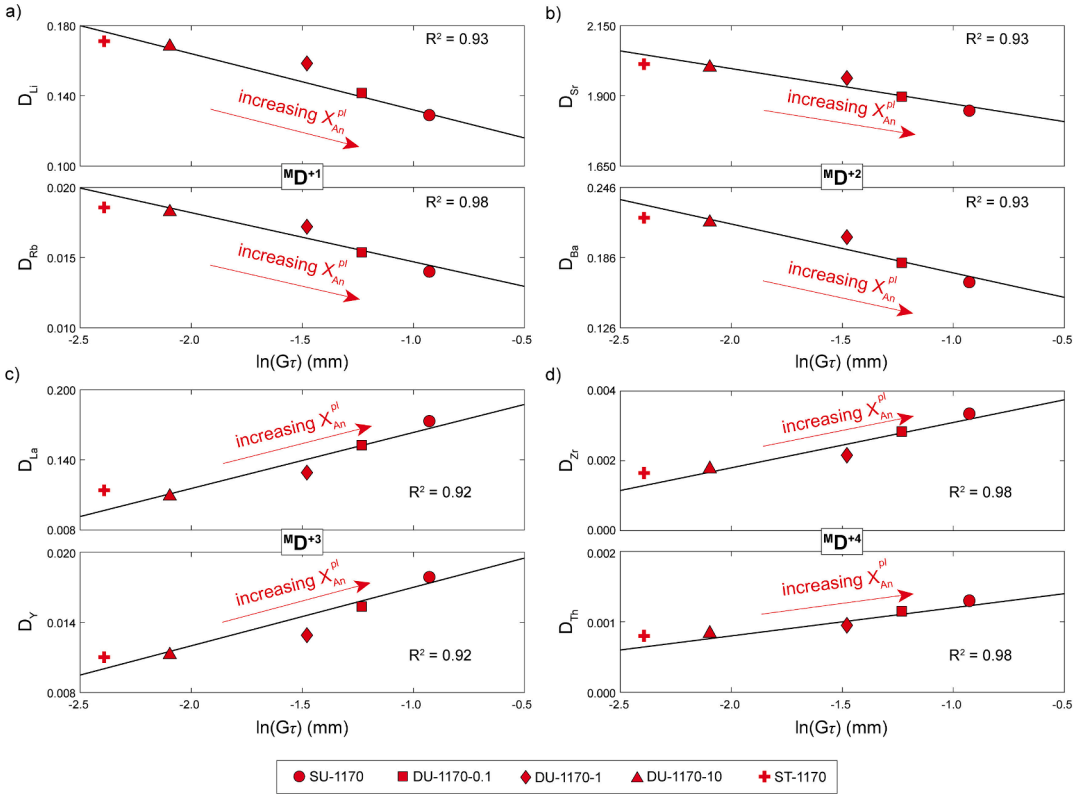

Fig. 5. The textural attribute ln($G\tau$) obtained for static and dynamic crystallization experiments is plotted against the partition coefficients $^{M}D_i^{+1}$ (a), $^{M}D_i^{+2}$ (b), $^{M}D_i^{+3}$ (c), and $^{M}D_i^{+3}$ (d) calculated for trace cations hosted into the M−site of plagioclase.

Fig. 5 shows representative values for ${}^{M}D_i^{+1}$ (D_{Li} and D_{Rb}), ${}^{M}D_i^{+2}$ (D_{Sr} and D_{Ba}), ${}^{M}D_i^{+3}$ (D_{La} and D_Y), and ${}^{M}D_i^{+4}$ (D_{Zr} and D_{Th}) plotted against ln ($G\tau$) as a function of static and dynamic crystallization conditions. All these plots are associated with a good linear correlation (R^2 = 0.92–0.98) that reflects the control exercised by the growth process on the composition of plagioclase, in particular X_{An}^{pl} as displayed in Fig. 4a. Similarly to the Ca-Na exchange partition coefficient, kinetic effects contribute to the deviation of trace element partition coefficients calculated for both static undercooling (*SU-1170*) and dynamic undercooling (*DU-1170–0.1–1-10*) experiments compared to those calculated for the equilibrium experiment (*ST-1170*). The absence of convective transport in *SU-1170* results in the dominant effect of melt undercooling, leading to large deviations from the equilibrium partition coefficients measured for *ST-1170* (Fig. 5). In contrast, convective mass transfer in *DU-1170–0.1–1-10* fosters chemical homogenization between the freshly deposited crystalline layer and the composition of the melt portion right adjacent to this layer. Consequently, the attachment and detachment of trace cations at the crystal-melt interface progress at slower reaction rates with increasing stirring. This causes the partition coefficients for *DU-1170–0.1–1-10* to gradually approach the nominal equilibrium values measured for *ST-1170* as $\dot{\gamma}$ increases from 0.1 to 10 s^{-1} (Fig. 5).

For ${}^{M}D_i^{+1}$ (Fig. 5a) and ${}^{M}D_i^{+2}$ (Fig. 5b), the value of partition coefficient decreases with increasing ln($G\tau$), denoting that ${}^{M}i^{1+}$ and ${}^{M}i^{2+}$ are more compatible in slow-growing, An^{pl}-poor crystals than fast-growing, An^{pl}-rich ones. The partitioning order of monovalent cations is D_{Li} (0.129–0.171) > D_{Rb} (0.014–0.019) > D_{Cs} (0.0004–0.0005). Assuming that charge balance criteria are respected in the M−site between trace and major host cations, Cs is likely more incompatible than Li due to its larger size compared to that of Na (i.e., r_{Li} = 0.92, r_{Na} = 1.18 Å, and r_{Cs} = 1.74 Å). For divalent cations, it is found that D_{Sr} (1.847–2.013) > D_{Ba} (0.165–0.220) > D_{Zn} (0.078–0.107). Among all the trace cations investigated, Sr is the only cation compatible with the lattice site of plagioclase and is more favorably incorporated in slow-growing, An^{pl}-poor crystals because of the greater elasticity and more flexible structure of Ab^{pl} with respect to An^{pl} (Blundy and Wood; 1991).

For ${}^{M}D_i^{+3}$ (Fig. 5c) and ${}^{M}D_i^{+4}$ (Fig. 5d), the value of partition coefficient increases with increasing ln($G\tau$). REE+Y are incompatible with plagioclase (D_{REE+Y} = 0.004–0.173) in response to the charge mismatch between ${}^{M}i^{3+}$ and both major Na and Ca substituting cations within the lattice site (Kneip and Liebau, 1994; Bindeman and Davis, 2000; Dohmen and Blundy, 2014; Sun et al., 2017; Bédard, 2023). As the atomic number increases and cation size decreases, partition coefficients decrease from light to heavy REE+Y. D_{LREE} (0.173–0.016) measured for light REE (LREE = La → Gd) with a larger size (r_{LREE} = 1.16–1.053 Å) are one-two orders of magnitude higher than those of D_{HREE} (0.028–0.004) measured for heavy REE (HREE = Tb → Lu) with a smaller size (r_{HREE} = 1.04–0.977 Å). Y has also a relatively small ionic radius (r_Y = 1.019) and behaves like a HREE. This suggests that the magnitude of D_{REE+Y} depends on the size of the ideal structural site, which is expected to be close to the ionic radius of the major host Na and Ca cations. According to Sun et al. (2017), tetravalent HFSE and actinides can be also hosted into the M−site of plagioclase, as for the case of REE+Y. However, values measured for D_{Hf}, D_{Zr}, D_U, and D_{Th} (0.001–0.034) are comparatively much lower than D_{REE+Y}, given that HFSE have higher charge and smaller ionic radii ($r_{Hf,\ Zr,\ U,\ Th}$ = 0.83–1.05 Å) compared to REE+Y.

Fig. S1 shows that ${}^{T}D_i^{+3}$ (D_{Ga} and D_{Sc}) and ${}^{T}D_i^{+4}$ (D_{Ge}) are positively correlated (R^2 = 0.90) with ln($G\tau$). D_{Sc} (0.032–0.049) is one order of magnitude more incompatible than D_{Ga} (0.534–0.813) (Fig. S1a), likely due to the size control on cation partitioning. The uptake of ${}^{T}i^{3+}$ onto the T-site of fast-growing, An^{pl}-rich crystals accounts for the increased proportion of tetrahedral aluminium and the ensuing expansion of Si-Al framework (see discussion below). On the other hand, following the charge-balanced reaction [${}^{M}Na^{1+}$] + [${}^{T}Si^{4+}$] ⇔ [$2{}^{M}Ca^{2+}$] + [${}^{T}Al^{3+}$] and the charge mismatch between ${}^{T}i^{4+}$ and ${}^{T}Al^{3+}$, Ge is less favorably incorporated into the T-site. Thus, D_{Ge} decreases from 0.392 to 0.308 with increasing ln($G\tau$) (Fig. S1b).

4. Discussion

4.1. Onuma plots and comparison of cation partitioning with the literature models

Onuma curves (Onuma et al., 1968) are obtained for groups of isovalent major (i.e., Ca, Na, and K), minor (i.e., Mg), and trace cations (i.e., Li, Rb, Cs, Zn, Sr, Ba, REE+Y, Hf, Zr, U, and Th) hosted into the M−site of plagioclase. For each Onuma diagram, ${}^{M}D_i^{+1}$, ${}^{M}D_i^{+2}$, ${}^{M}D_i^{+3}$, and ${}^{M}D_i^{+4}$ are plotted against the radius of the corresponding cation. Fig. 6 shows an example of Onuma curve derived for data from *SU-1170*, whilst plots for all the experiments are comparatively illustrated in Fig. S2. Partition coefficients from this study are also compared with those predicted by equilibrium partitioning models from literature (hereafter M_{1991} from Blundy and Wood, 1991, M_{1998} from Bindeman et al., 1998, M_{2000} from Bindeman and Davis, 2000, M_{2006} from Bédard, 2006, M_{2010} from Tepley et al., 2010, M_{2014} from Dohmen and Blundy, 2014, M_{N2017} from Nielsen et al., 2017, M_{S2017} from Sun et al., 2017, M_{2022} from Mutch et al., 2022, and M_{2023} from Bédard, 2023). All modeling results are reported in the Supplementary Material. To quantitatively treat this comparison, the percentage deviation is calculated as $\Delta D\% = (|D_{measured} - D_{modeled}|/D_{measured}) \times 100$ (Supplementary Material).

For ${}^{M}D_i^{+1}$, M_{2014} reproduces the experimental data set for D_{Li}, D_{Na}, and D_K ($\Delta D\%_{0\text{-}47}$) moderately well, but larger deviations are observed for D_{Rb} ($\Delta D\%_{44\text{-}50}$) and D_{Cs} ($\Delta D\%_{59\text{-}66}$). The best models for D_{Na} ($\Delta D\%_{9\text{-}13}$) and D_{Rb} ($\Delta D\%_{2\text{-}6}$) correspond to M_{1998} and M_{2010}, respectively (Figs. 6 and S2). Partition coefficients calculated for Na and Li (both considered volatile elements) closely align with the Onuma fit determined for monovalent cations. This suggests that any devolatilization effect, if present, was negligible throughout the experimental duration. In previous partitioning studies, no Na loss has been detected in glass compositions containing up to ~12 wt% Na_2O, even after annealing treatments ranging from 1 week to 70 days (Bindeman et al., 1998; Bindeman and Davis, 2000; Dohmen and Blundy, 2014). Most of the modeled partition coefficients are negatively correlated with X_{An}^{pl}, in accord with our experimental data set (Supplementary Material). Trace cations enter the lattice site of plagioclase crystals by the homovalent substitution [${}^{M}Na^{1+}$] ⇔ [${}^{M}i^{1+}$] taking place when An^{pl}-poor crystals develop with increasing $\dot{\gamma}$ at the constant temperature of 1,170 °C. However, a thermodynamically implausible positive relation between ${}^{M}D_i^{+1}$ and X_{An}^{pl} is found for M_{S2017} and M_{2023} because the calibration criteria of these models are satisfied when T and X_{An}^{pl} concurrently change during melt crystallization. Therefore, growth kinetics in our experiments generates artefacts for the estimate of ${}^{M}D_i^{+1}$ as X_{An}^{pl} decreases without the need to change the system temperature.

For ${}^{M}D_i^{+2}$, model predictions provide close estimates for D_{Mg} ($\Delta D\%_{2\text{-}37}$ from M_{2014} and M_{2022}), D_{Ca} ($\Delta D\%_{3\text{-}9}$ from M_{1998}), D_{Sr} ($\Delta D\%_{1\text{-}14}$ from M_{2006} and M_{2014}), and D_{Ba} ($\Delta D\%_{3\text{-}16}$ from M_{1991}, M_{2006}, M_{2010}, M_{2014}, and M_{2023}). D_{Sr} and D_{Ba} decrease with decreasing X_{An}^{pl} in both measured and modeled partition coefficients (Supplementary Material). Because the size of the M−site in Ab^{pl} is larger than that in An^{pl}, the component $NaAlSi_3O_8$ has a greater capacity to accommodate i^{2+} misfit cations via the coupled exchange [${}^{M}Na^{1+}$] + [${}^{T}Si^{4+}$] ⇔ [${}^{M}i^{2+}$] + [${}^{T}Al^{3+}$] (Blundy and Wood, 1991). The only exception to such cation incorporation reaction is found using M_{2006}, which returns a counterintuitive increase of D_{Sr} with decreasing X_{An}^{pl} (Supplementary Material). As discussed above, this artefact is due to the isothermal compositional dependence of D_{Sr} on Ab^{pl}-An^{pl} solid solution upon the effect of growth kinetics instead of the control of equilibration temperature on cation partitioning. Values of

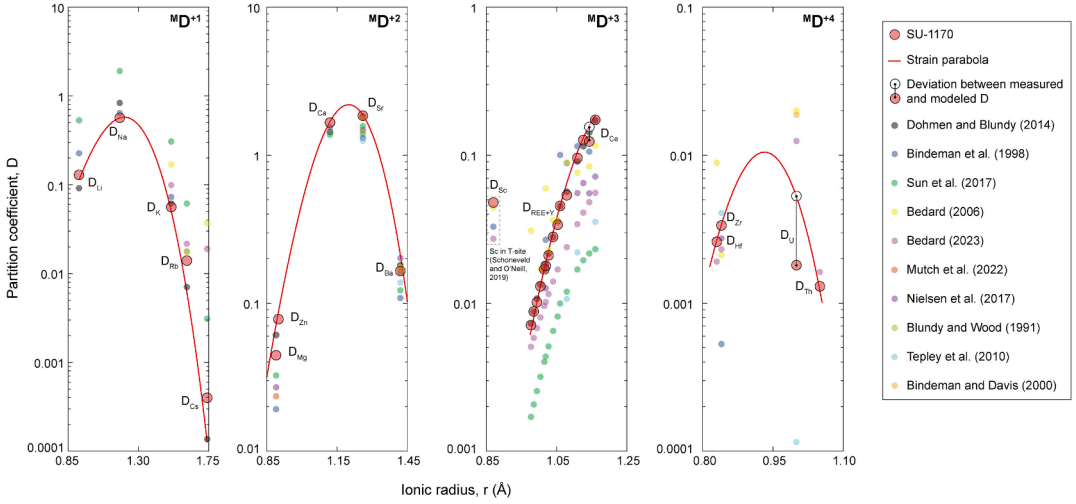

Fig. 6. Example of Onuma diagram for *SU-1170*, where the partition coefficients $^{M}D_i^{+1}$, $^{M}D_i^{+2}$, $^{M}D_i^{+3}$, and $^{M}D_i^{+4}$ are plotted against the radius *r* of the corresponding cation. The experimental data set is compared with estimates from a range of equilibrium partitioning models from literature (see the text for details). Parabolic fits are obtained using the lattice strain model of Blundy and Wood (1994). Plots for all the experiments from this study are comparatively illustrated in Fig. S2.

D_{Mg} from M_{1998}, M_{N2017}, and M_{2022} decrease with decreasing X_{An}^{pl}. In contrast, D_{Mg} from M_{2014} is observed to increase or, alternatively, to remain almost constant in using M_{S2017} (Supplementary Material). Comparatively, measured values for D_{Mg}, D_{Zn}, D_{Ba}, and D_{Sr} mutually decrease with increasing X_{An}^{pl} (Fig. 5 and Supplementary Material), pointing out that the entry of i^{2+} misfit cations into the lattice site of plagioclase is determined by an abrupt change in the activity coefficients of Ab^{pl}-An^{pl} solid solution components (Drake and Weill, 1975). This thermodynamic factor accounts for the well-defined parabolic patterns obtained for $^{M}D_i^{+2}$ from this study (Fig. 5 and Supplementary Material) and from a range of literature experiments, in which An^{pl}-rich plagioclase crystals are equilibrated with high-*T*, magnesian melts (e.g., Blundy and Wood, 1994; Dohmen and Blundy, 2014; Sun et al., 2017).

For $^{M}D_i^{+3}$, all partition coefficients measured for D_{REE+Y} are within $\Delta D\%_{0\text{-}23}$ of the estimates from M_{2014} (Figs. 6 and S2). The fraction of Ce^{3+} is expected to be low at air redox conditions, leading to a cation deficiency that results in a positive deviation of D_{Ce} from the Onuma fit (on the order of 15–27%, as illustrated in Figs. 6 and S2). Conversely, the good correspondence between D_{Eu} and the Onuma parabola indicates the predominance of Eu^{3+} over Eu^{2+} (Figs. 6 and S2). As observed by Drake and Weill (1975), the concentration of Eu^{3+} in plagioclase closely corresponds to the linear interpolation between Sm and Gd under highly oxidizing conditions. By exploring different thermodynamic criteria for the partitioning of REE+Y between plagioclase and melt, Dohmen and Blundy (2014) emphasize the importance of thermodynamic relations to isolate the effect of *T* from that of crystal and melt compositions. The small deviation between measured and modeled values of D_{REE+Y} suggests that M_{2014} legitimately deconvolves the influence exercised by *T* and X_{An}^{pl} on the kinetic partitioning of REE+Y. Among all the models from literature, M_{2014} best describes the experimental partitioning data set because its thermodynamic formalism accounts for compositional effects arising from pseudo-ideality and/or non-ideality between plagioclase and melt components, when the *P*-*T* conditions of the system are kept constant. As explained by Dohmen and Blundy (2014), when the effects of temperature and bulk system composition are isolated and considered separately, M_{2014} predicts a counterintuitive behavior in which D_{REE+Y} tends to increase with increasing *T* (or alternatively X_{An}^{pl}) due to the counteracting influence of melt chemistry on cation partitioning. Some other models based on the regression analysis of experimental data perform moderately well with D_{La} and D_{Ce} ($\Delta D\%_{3\text{-}33}$ from M_{2006}), and D_{Gd}, D_{Tb}, D_{Dy}, D_Y, D_{Ho}, and D_{Er} ($\Delta D\%_{1\text{-}50}$ from M_{2023}). On crystallochemical grounds, however, these regression equations define a negative correlation between D_{REE+Y} and X_{An}^{pl}, provided that the amount of An^{pl} is modeled to substantially increase upon the dominant control of the system temperature (Supplementary Material). From this perspective, the equilibrium growth of plagioclase at constant melt-H_2O content requires the formation of more anorthitic crystals at higher temperatures. Since X_{An}^{pl} and *T* are closely interdependent, the equilibrium value of D_{REE+Y} decreases with increasing X_{An}^{pl} (e.g., Bédard, 2023), consistent with the positive enthalpy (ΔH_{fusion}) and entropy (ΔS_{fusion}) of fusion of common igneous minerals (Wood and Blundy, 2001; Blundy and Wood, 2003a, 2003b). At higher temperatures, the Gibbs free energy change (i.e., $\Delta G_{fusion} = \Delta H_{fusion} - T\Delta S_{fusion}$) becomes more negative because the term $T\Delta S_{fusion}$ increases much more significantly compared to ΔH_{fusion} (i.e., $T\Delta S_{fusion} \gg \Delta H_{fusion}$). As the process becomes more thermodynamically favorable with increasing temperature, trace cations are less likely to be incorporated into the solid mineral and are instead more likely to remain in the melt (Wood and Blundy, 2001; Blundy and Wood, 2003a, 2003b). In contrast, in our kinetic experiments, the magnitude of D_{REE+Y} is no longer primarily determined by the increase of $T\Delta S_{fusion}$, as the growth of plagioclase proceeds at the constant temperature of 1,170 °C. Thus, interface kinetics are critical for enhancing the incorporation *REE*+*Y* into more anorthitic and rapidly growing crystals, with the increase of X_{An}^{pl} being driven solely by the combined effects of melt supersaturation and convective stirring. From an energetic point of view, several substitution reactions may account for the uptake of REE+Y into the M−site of plagioclase (Kneip and Liebau, 1994; Bindeman and Davis, 2000; Dohmen and Blundy, 2014; Sun et al., 2017; Schoneveld and O'Neill, 2019; Bédard, 2023). Complete short-range order between trivalent cations in the M−site and tetrahedral aluminium may conveniently contribute to the component $^{M}i^{3+}Al_3SiO_8$ for the solution of REE+Y into anorthitic crystals (Schoneveld and O'Neill, 2019). Several works (Wood and Banno, 1973; Wood, 1976; Wood et al., 1980) have illustrated that heterovalent cation substitution reactions are accompanied by a similar increase of ΔH_{mix} and $T\Delta S_{mix}$, with the result that ΔG_{mix} remains nearly the same due to achievement of charge-neutral local configurations associated with Al-O-Al linkages in the short-range structural arrangement of the lattice. A similar crystal-chemical control is documented for the increased probability of REE+Y to enter a locally charge-balanced site of clinopyroxene (Blundy and Wood, 2003a, 2003b; Wood and Blundy, 2001, 2003; Mollo et al., 2018, 2020). It is also worth mentioning that size distortions caused by the entry of REE+Y in the crystal structure are energetically minimized at high-

temperature, especially for aluminosilicate minerals characterized by weak T-O bonds and a low Al-Si exchange activation energy (Navrotsky, 1978; Kneip and Liebau, 1994).

In Figs. 6 and S2, D_{Sc} is plotted together with D_{REE+Y} accounting for the VIII-fold coordinated ionic radius of scandium (0.87 Å), as reported in Shannon (1976). D_{Sc} is reproduced quite well by M_{2006} ($\Delta D\%_{9\text{-}37}$) and with less precision by M_{2023} ($\Delta D\%_{16\text{-}44}$). Note that measured and modeled values of D_{Sc} do not align with the Onuma parabola derived for D_{REE+Y}, suggesting partitioning into a different site. Our plot resembles that proposed by Schoneveld and O'Neill (2019) for trace element partitioning between anorthitic crystals and simplified CAS ($CaO\text{-}Al_2O_3\text{-}SiO_2$) and CMAS ($CaO\text{-}MgO\text{-}Al_2O_3\text{-}SiO_2$) melts. Although there is no quantitative information in literature for the ionic radius of scandium in IV-fold coordination, the experimental data set presented here supports the proposition of Schoneveld and O'Neill (2019) that scandium substitutes onto the T-site of plagioclase in place of aluminium, likely to form the fictive component $CaScAlSi_2O_8$.

For ${}^{M}D_i^{+4}$, M_{2023} captures reasonably well the variance of D_{Hf} ($\Delta D\%_{14\text{-}58}$) and D_{Zr} ($\Delta D\%_{1\text{-}31}$), whereas moderate to very large deviations between measured and modeled partition coefficients are calculated for D_{Th} ($\Delta D\%_{25\text{-}85}$) and D_U ($\Delta D\%_{520\text{-}1022}$), respectively. As observed for other multivalent cations, a fraction of U^{4+} is oxidized to U^{5+}-U^{6+} and these highly charged trace cations are less favorably incorporated into the lattice site of plagioclase (de Vries et al., 2012; Sun et al., 2017; Schoneveld and O'Neill, 2019). This elucidates why the measured values of D_U (which were not used for the fit of ${}^{M}D_i^{+4}$) are lower (0.001–0.002) than the ideal values (0.003–0.005) derived by minimizing the residuals (i.e., the sum of the squares of the offsets) of the best fitting Onuma curves (Figs. 6 and S2). Despite the oxidative effect of air on melt composition, the overall values measured for ${}^{M}D_i^{+4}$ increase with increasing X_{An}^{pl} according to modeling results from M_{2023}. A positive D_{Zr}-X_{An}^{pl} relation is also documented by Aigner-Torres et al. (2007) for atmospheric pressure experiments caried out on a MORB equilibrated from 1,180 to 1,220 °C at $\log fO_2 \approx -0.68$.

Regarding major (i.e., Al^{3+} and Si^{4+}), minor (i.e., Fe^{3+} and Ti^{4+}), and trace (i.e., Ga^{3+} and Ge^{4+}) cations hosted into the T-site of plagioclase, we do not have enough data to quantitatively fit the Onuma parabola, given that only three values for ${}^{T}D_i^{+3+}$ and ${}^{T}D_i^{+4}$ are distributed on the same side of the parabolic limb. Despite this limitation, the alignments of isovalent partition coefficients depict putative parabolic patterns in Onuma plots displayed in Fig. S3. D_{Ga} is well reproduced by M_{2023} ($\Delta D\%_{1\text{-}27}$), defining a positive dependence of D_{Ga} on X_{An}^{pl}. Both Ga and Fe^{3+} are likely hosted into the T-site of plagioclase owing to their similar ionic radii ($r_{Ga} = 0.47$ Å and $r_{Fe} = 0.49$ Å) and the dominance of ferric iron in the oxidized experiments. This crystal-chemical criterion is thought to control the homovalent exchange $[{}^{T}Al^{3+}] \Leftrightarrow [{}^{T}i^{3+}]$ and the stabilization of the fictive component $Ca(Al^{3+}, i^{3+})Si_2O_8$ (Longhi et al., 1976; Bindeman et al., 1998; Wilke and Behrens, 1999; Aigner-Torres et al., 2007). On the other hand, D_{Ge} and D_{Ti} decrease with increasing X_{An}^{pl}, as modeled by M_{2006} ($\Delta D\%_{3\text{-}31}$) and M_{2023} ($\Delta D\%_{0\text{-}4}$), respectively. The partitioning of Ti also matches with estimates from M_{1998} ($\Delta D\%_{3\text{-}12}$) and M_{N2017} ($\Delta D\%_{11\text{-}21}$) but these models are slightly less precise than M_{2023}. Because Ge and Ti have comparable ionic radii (0.39 and 0.42 Å, respectively), their entry into the T-site of plagioclase is mainly governed by the homovalent exchange $[{}^{T}Si^{4+}] \Leftrightarrow [{}^{T}i^{4+}]$ for the fictive component $CaAl_2(Si^{4+}, i^{4+})O_8$ (Bindeman et al., 1998; Miller et al., 2006; Aigner-Torres et al., 2007).

The overriding implication of Onuma diagrams displayed in Figs. 6 and S2 is that isovalent groups of D_i from *SU-1170*, *DU-1170–0.1–1–10*, and *ST-1170* unequivocally depict explicit parabolic patterns. These partitioning parabolas, although influenced by kinetic effects, share a topological equivalence with those derived by equilibrium models that rely on isothermal compositional dependence of D_i on X_{An}^{pl}, wherein the influence of temperature is opportunely deconvoluted from the change of Ab^{pl}-An^{pl} solid solution imposed by the crystallization regime. Therefore, the partitioning energetics of major, minor, and trace cations are embodied into the thermodynamic and kinetic aspects of plagioclase growth (compare Figs. 4a and 5). Adherence of isovalent partition coefficients to parabolic variations also excludes trapping of small amounts of melt into the crystalline material via a disequilibrium growth process. As outlined by a number of previous works (cf. Kennedy et al., 1993; Lofgren et al., 2006; Mollo et al., 2013, 2023), any sort of intracrystalline heterogeneity and contamination due to random incorporation of small amounts of melt into the crystalline material during LA-ICP-MS analysis would produce a set of partition coefficients that are independent of cation charge and radius (see for example distortions of Onuma parabolas modeled as a function of analytical contamination in Fig. S3 of Mollo et al., 2023).

4.2. Lattice strain parameterization upon plagioclase growth kinetics

The lattice strain model formulated in the cardinal study of Blundy and Wood (1994) relates D_i with the thermodynamic and crystallochemical properties of the host crystal as:

$$D_i = D_0 exp\left\{\frac{-4\pi E N_A\left[\frac{r_0}{2}(r_i - r_0)^2 + \frac{1}{3}(r_i - r_0)^3\right]}{RT}\right\} \quad (2)$$

where N_A is the Avogadro's number, R is the gas constant, T is the system temperature, and r_i is the ionic radius of the cation of interest. D_0, E, and r_0 from Eq. (2) are the lattice strain parameters governing the magnitude of ΔG_{strain}. The parameter r_0 represents the strain-free ionic radius when a substituting trace cation enters the crystallographic site without strain. At this minimum energetic condition, r_0 intersects the apex of the partitioning parabola at the strain-free partition coefficient D_0, defining the height of the curve (Figs. 6 and S2). The strain produced by insertion of misfit trace cations in the lattice site is proportional to the curvature of the parabola, which is algebraically controlled by the apparent Young's modulus E. The curve becomes more open as the distance between its left- and right-hand limbs increases in response to the increased elasticity of the crystallographic site at lower values of E (Figs. 6 and S2). As stated above, parabola-like curves are quantified only for major, minor, and trace cations hosted into the M−site of plagioclase. The data set includes either a large number of partition coefficients constraining very well the left-hand limb of the expected parabola (i.e., ${}^{M}D_i^{+3}$) or a more restricted number of partition coefficients that define both the left- and right-hand limbs (i.e., ${}^{M}D_i^{+1}$, ${}^{M}D_i^{+2}$, and ${}^{M}D_i^{+4}$), which are two prerequisites essential to minimize the error associated with the regression approximation. Through a Levenberg–Marquardt-type, non-linear least-squares fitting routine, the best-fit lattice strain parameters are derived by weighting the fits using σ_D of partition coefficients measured for *SU-1170*, *DU-1170–0.1–1-10*, and *ST-1170* (Supplementary Material).

In Fig. 7, values derived for D_0, E, and r_0 are compared with the corresponding variation of $\ln(G\tau)$, as a proxy for interface kinetics driving the textural evolution of plagioclase. D_0^{+1} decreases by ~25% as $\ln(G\tau)$ increases. In contrast, D_0^{+2} decreases by only ~2% in response to the little variation measured for D_{Ca} (~7%) and the dominance of the host major Ca cation into the M−site of plagioclase. The stability of ${}^{M}i^{3+}Al_3SiO_8$ component into more anorthitic crystals determines the increase of D_0^{+3} by ~25% as a function of $\ln(G\tau)$. Because trace elements are non-essential structural constituents at high dilution, REE+Y are accommodated into the larger interstices of the three-dimensional framework of bonded (Si, Al)-O tetrahedra by charge-neutral local configurations, in which the valence of charge-balancing cations in nearest-neighbor sites changes to produce a statistical proportion of sites with central cations having charge 3+ rather than 2+ (Wood, 1976; Wood and Blundy, 2001, 2003a, 2003b; Wood and Blundy, 2003).

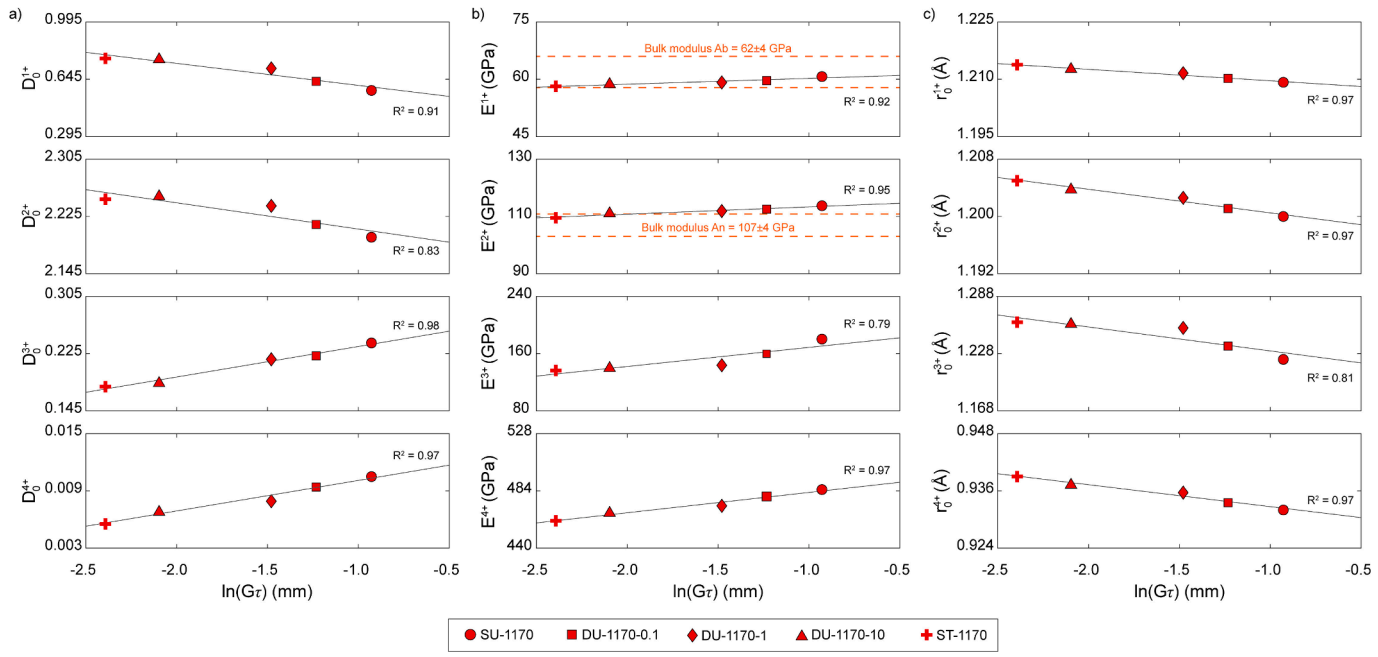

Fig. 7. The lattice-strain parameters D_0 (a), E (b), and r_0 (c) are compared with the textural attribute ln($G\tau$).

Following the same principle, D_0^{+4} greatly increases by 47% due to an increased ease of locally balancing the excess charge at the M−site, as the number of surrounding ^{T}Al increases in the hypothetical component $^{M}i^{4+}Al_4O_8$ via the charge-balanced reaction [$^{M}Ca^{2+}$] + [$2^{T}Si^{4+}$] ⇔ [$^{M}i^{4+}$] + [$2^{T}Al^{3+}$]. In line with previous partitioning studies (Mollo et al., 2013; Lang et al., 2021, 2022; MacDonald et al., 2022; Di Fiore et al., 2023), kinetic incorporation of trace cations in the lattice site proceeds by the attainment local interface equilibrium (i.e., equilibrium of a reaction in a small volume), while the overall Ab^{pl}-An^{pl} solid solution of plagioclase departs from the macroscopic equilibrium state of the system. This mechanism enhances the stability of different local configurations into the plagioclase structure, thereby increasing the probability for high charge density trace cations to enter a locally charge-balanced site under kinetically-controlled crystallization conditions.

In general, the Young's modulus E is found to increase at higher values of ln($G\tau$) (Fig. 7b), mainly in response to the increase of X_{An}^{pl} (Fig. 4a) and the more rigid structure of An^{pl} compared to Ab^{pl} (Blundy and Wood, 1991). However, as previously observed by Dohmen and Blundy (2014), both E^{+1} and E^{+2} increase by only ~4%, with a physical significance that approximates to the Young's moduli of bulk Ab^{pl} (62 ± 4 GPa) and bulk An^{pl} (107 ± 4 GPa), as calculated by Blundy and Wood (1991) for homovalent cation substitutions. A similar small variation is also observed for E^{+4} (~4%), whereas E^{+3} moderately increases (~25%) likely due to an excess of strain required to accommodate REE+Y into the lattice site of plagioclase (Blundy and Wood, 2003a, 2003b; Wood and Blundy, 2003).

Values of r_0 slightly decrease with increasing ln($G\tau$) (Fig. 7c), with trends that are opposite to those depicted by E (Fig. 7b). The parameterization proposed by Dohmen and Blundy (2014) indicates a similar negative correlation between the optimum ionic radius and Young's modulus, as r_0^{+1}, r_0^{+2}, and r_0^{+3} mutually decrease with increasing X_{An}^{pl}. At the same time, the regression equations reported in Blundy and Wood (2003b) and Sun et al. (2017) estimate a decrease of r_0^{+2} for the fast-growing, An^{pl}-rich plagioclase crystals. All these modeled values compare well with those measured in this study within a percentage deviation of only 0.1–4.1%, also denoting a progressive change of the interatomic distances across the Ab^{pl}-An^{pl} solid solution. In particular, <Al-O> interatomic distances are ~0.13 Å longer than <Si-O> in the structural site of plagioclase, therefore the increase of X_{An}^{pl} in plagioclase is associated with expansion of the T-site and consequent contraction of the M−site in which REE+Y are more favorably incorporated (Ribbe, 1983).

4.3. Dependence D_0 on the activities of melt and plagioclase components

The lattice strain model assumes that trace cations behave as charged point defects in a dielectric and elastic continuum medium. At this condition, there is no surplus of elastic energy and the strain-free partition coefficient is suggested to depend on activity-composition relations in both melt and crystal phases, provided that $\Delta G_{exchange}$ is divided into a non-ideal part ΔH_{mix} and an ideal counterpart ΔS_{mix} (Blundy et al., 1996). ΔH_{mix} represents the structural work required to accommodate misfit cations and is essentially dominated by ΔG_{strain}. Conversely, ΔS_{mix} is mainly related to the difference in configurational entropy between plagioclase and melt. S_{conf} is a molar property of end-member components in the solution, arising from the distribution of atoms in their structures and remaining constant with T as long as the configuration of atoms between different structural sites does not change. Thus, ΔS_{mix} depends on both melt and crystal compositions, any concentration effect contributing to the accommodation of charge-balancing cations, and the number of structural configurations required to the solution of a fictive trace element component into a host major component (Blundy et al., 1996). Following these considerations, it is important to evaluate whether appreciable compositional dependence remains for D_0 in relation to activity models derived for melt and plagioclase components.

For the melt counterpart, the thermodynamic treatment used for relating the activities of melt major oxide components (i.e., $a_{AlO_{1.5}}^{melt}$ of $a_{SiO_2}^{melt}$) to the partition coefficients of trace cations (i.e., $^{M}i^{1+}$, $^{M}i^{2+}$, $^{M}i^{3+}$, and $^{M}i^{4+}$) is described in more detail in the Supplementary Material. In brief, this thermodynamic treatment is grounded in prior studies on homovalent and heterovalent exchange reactions (Miller et al., 2006; Dohmen and Blundy, 2014; Sun et al., 2017; Schoneveld and O'Neill, 2019), as well as on the Gibbs free energy change that defines the equilibrium constant of a trace cation partitioning between crystal and melt (Wood and Blundy, 2003). Activities of SiO_2 and $AlO_{1.5}$ are derived from the thermodynamic model of Moschini et al. (2023), describing the composition-related non-ideality of multicomponent mafic alkaline

melts through a symmetric regular solution type equation (Supplementary Material). The activity products of partitioning equations are plotted against D_0^{+1}, D_0^{+2}, D_0^{+3}, and D_0^{+4} in Fig. 8a. For cations with low charge densities (i.e., $^{M}i^{1+}$ and $^{M}i^{2+}$), there is an increasing availability to form cation-oxygen polyhedra in the silicate melt with increasing network-forming cations (Ryerson and Hess, 1978), thereby explaining the anticorrelation between the strain-free partition coefficients (i.e., D_0^{1+} and D_0^{2+}) and the melt activity products. The goodness of fits illustrated in Fig. 8a ($R^2 = 0.89–1.00$) outlines that the effect of interface melt on cation partitioning cannot be entirely deconvoluted from the structural changes of the crystal lattice for a range of mineral solid solutions, also in line with thermodynamic modeling of phase equilibrium data from previous works (O'Neill and Eggins, 2002; Gaetani, 2004; Miller et al., 2006; Schoneveld and O'Neill, 2019; Di Stefano et al., 2019; Mollo et al., 2020). In essence, the term D_0 of Eq. (2) represents a simple-activity composition model for the crystal but other effects collateral to melt thermodynamics are not accounted for. S_{conf} may provide a dominant contribution to the entropy of melting reaction of fictive trace element components, and on physical grounds, it is likely that $\Delta S_{mix} \approx S_{conf}$ when different atoms redistribute themselves among lattice points and interstitial sites due to loss of long-range order. Within this conceptual framework, the algebraic treatment of balanced chemical reactions displayed in Fig. 8a highlights that the parameterization of major component activities is proportional to the energy associated with the number of structural sites critically important to accommodate trace cations in the melt and, ultimately, the overall solution energy accompanying trace cation partitioning (e.g., Miller et al., 2006).

For the plagioclase counterpart, the activities of Ab^{pl}-An^{pl} solid solution components are comparatively calculated using Models 1, 2, and 4 (i.e., $M1_{1975}$, $M2_{1975}$, and $M4_{1975}$, respectively) described in Kerrick and Darken (1975) and based on a rigorous treatment of statistical mechanics. Ideal activity expressions for plagioclase components are derived with and without adherence to both Al-avoidance and local electroneutrality principles (Supplementary Material). It is worth noting that there is no numerical solution for Model 3 from Kerrick and Darken (1975). As a further investigation, Models 1, 2, 3, 4, and 5 (i.e., $M1_{1992}$, $M2_{1992}$, $M3_{1992}$, $M4_{1992}$, $M5_{1992}$, respectively) proposed by Holland and Powell (1992) and based on the Darken's quadratic formalism are also considered here (Supplementary Material). Fig. 8b shows an excellent linear relation ($R^2 = 0.91–1.00$) between $a_{AnM4_{1975}}^{pl}$ and $a_{AnM1_{1992}}^{pl}$ values and the measured strain-free partition coefficients. In both $M1_{1975}$ and $M2_{1992}$, a_{An}^{pl} approximates to X_{An}^{pl} within only 2% average deviation, according to random mixing on both M- and T-sites and hypothetical end-members of disordered Ab^{pl} and disordered An^{pl}. Replicate regression analysis for $a_{AnM1_{1975}}^{pl}$, $a_{AnM2_{1992}}^{pl}$, and $a_{AnM5_{1992}}^{pl}$ returns the same regression statistics ($R^2 = 0.91–1.00$) as those derived for the simplest solution models $M4_{1975}$ and $M1_{1992}$ displayed in Fig. 8b. This finding suggests that ions interact ideally within the individual structural sites, so that the overall variation of D_0 can be invariably described by

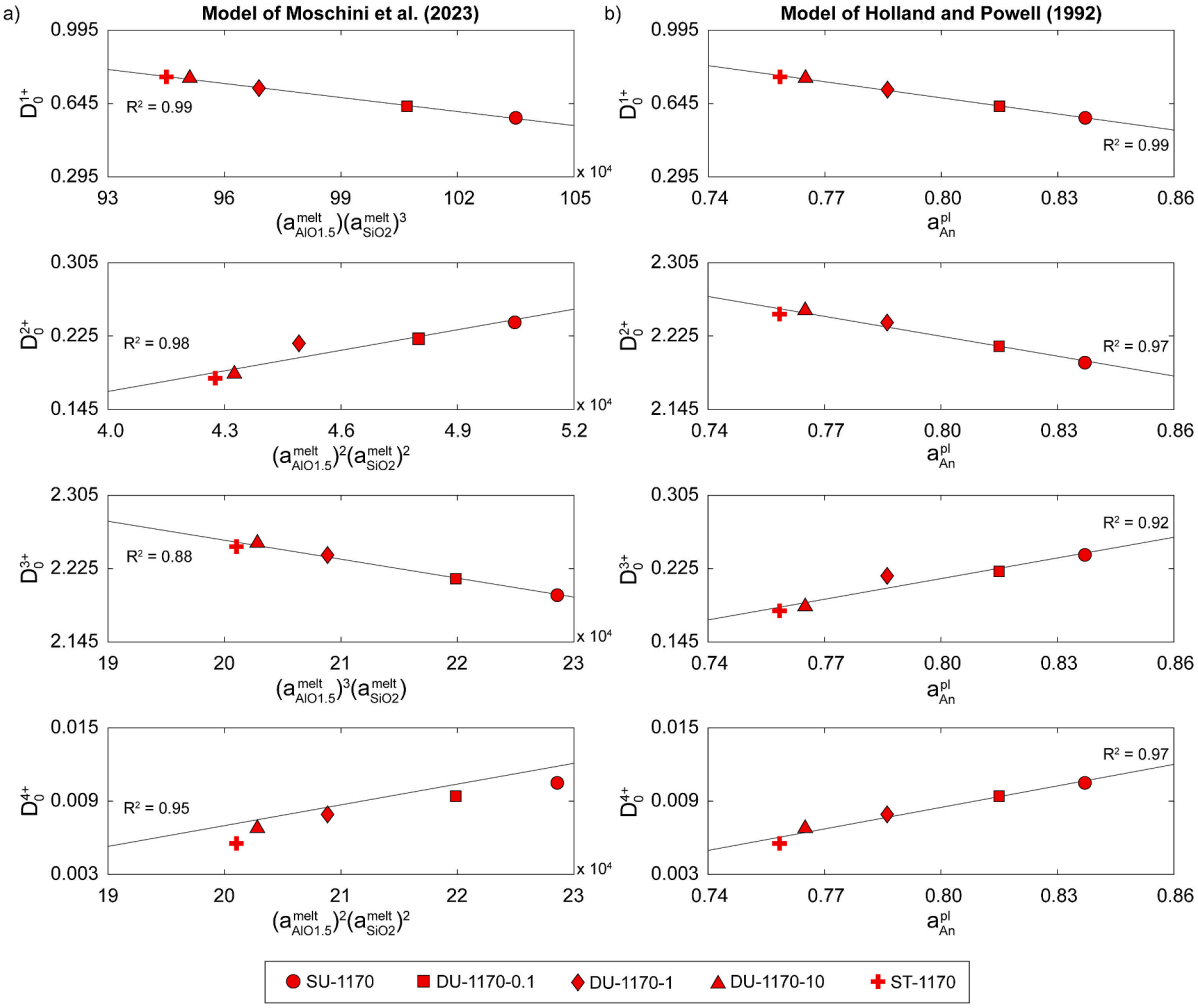

Fig. 8. The strain-free partition coefficients D_0^{1+}, D_0^{2+}, D_0^{3+}, and D_0^{4+} for static and dynamic experiments are compared with the activity products of melt major oxides from the model of Moschini et al. (2023) (a) and the activity of anorthite from the models $M4_{1975}$ and $M1_{1992}$ of Kerrick and Darken (1975) and Holland and Powell (1992), respectively (b).

thermodynamic formalisms derived for ideal and non-ideal mixtures of components in the plagioclase structure. The formation of Ab^{pl}-An^{pl} ordered domains is not irrelevant to high-temperature plagioclase crystals from static and dynamic experiments, as it conveys the message that plagioclase solid solution components behave nearly ideally due to independence of vibrational states on geometric configurations. Complete Al-Si mixing on the T-site with formation of Al-O-Al linkages does not contribute to the free energy of the Ab^{pl}-An^{pl} solid solution either enthalpically or entropically, leading to a pseudo-ideal activity-composition behavior of the solution (i.e., $\Delta G_{mix} \approx constant$; Wood and Banno, 1973; Wood, 1976; Wood et al., 1980).

The influence (I) exerted by the activity products of melt components (Fig. 8a) and the activity of plagioclase components (Fig. 8b) on the strain-free partition coefficient is quantified through the same standardized regression coefficient method used for illustrating the control of different compositional parameters on the partitioning of cations between clinopyroxene and melt (Mollo et al., 2018, 2020, 2023). In this statistical formulation, the original unstandardized regression coefficient of the independent variable (i.e., the strain-free partition coefficient) is multiplied by its standard deviation and divided by the standard deviation of each dependent variable (i.e., melt and crystal activity compositions). Results from calculations indicate that the overall variation of D_0^{+1}, D_0^{+2}, D_0^{+3}, and D_0^{+4} is axiomatically controlled by ~50% I^{melt} and ~50% I^{pl} for all the experimental conditions investigated. What we learn from this statistical analysis is that the melt and plagioclase compositions do not vary independently upon static and dynamic crystallization regimes. Therefore, the dependence of lattice strain parameters on plagioclase growth is influenced by the solution of anorthite and albite in the surface of the growing plagioclase face and the concurrent compositional variation of the adjacent melt.

4.4. Electrostatic parameterization upon plagioclase growth kinetics

Insertion of a trace cation with charge Z_i different from that of the cation resident in the crystallographic site Z_0 produces an excess of $\Delta G_{electrostatic}$ that is associated with electrostatic forces resulting from the displacement of nearest-neighbor ions in the charged region. If electrostatic work is done during cation partitioning, then D_0 for each isovalent group of trace elements depicts a parabolic dependence on Z_i (Wood and Blundy, 2001, 2003; Blundy and Wood, 2003a, 2003b). D_{00} corresponds to the apex of the parabola at r_i/r_0 and Z_i/Z_0 equal to 1, assuming that neither elastic strain nor electrostatic work are required for cation substitution. The electrostatic energy penalty is proportional to the radius ρ (in Å) of the region over which the excess charge is distributed and the dielectric constant ε of the undisturbed matrix lattice, ranging from 5 to 19 for silicates at room temperature. By analogy with the parabolic relationship developed for the lattice strain model, it follows that $\Delta G_{electrostatic}$ is embodied in the exponential term of the expression:

$$D_i = D_{00}\exp\left(\frac{-N_A e_0^2 (Z_i - Z_0)^2}{2\varepsilon\rho RT}\right) \quad (3)$$

where e_0 is the charge on the electron (1.6×10^{-19} C), whereas N_A, R, and T as for Eq. (2). The electrostatic parameter D_{00}, Z_0, and $\varepsilon\rho$ are calculated through the same non-linear least-squares routine used for Eq. (2) and are listed in the Supplementary Material. The resulting parabolic patterns are displayed for static and dynamic experiments in Fig. 9 and are ordered from left to right according to the decrease of both $\ln(G\tau)$ and X_{An}^{pl}. From *SU-1170* to *DU-1170–0.1–1–10* to *ST*-1170, D_0^{+3} and D_0^{+4} move downward along the right-hand limb of the electrostatic parabola, whereas D_0^{+1} moves upward along the left-hand limb. D_0^{+2} does not show marked variations at the logarithmic scale of Fig. 9 but its value approaches the vertex of the electrostatic parabola. The ratio of D_0^{+1}/D_0^{+3} and D_0^{+1}/D_0^{+4} increases up to 80% and 154%, respectively, and this different partitioning behavior contributes to the curvature of the electrostatic parabola that becomes more open moving from left to right in Fig. 9.

A linear dependence is found between all the electrostatic parameters and the textural/compositional parameters $\ln(G\tau)$ ($R^2 = 0.93$–0.98; Fig. 10a), a_{An}^{melt} ($R^2 = 0.90$–0.99; Fig. 10b), and a_{An}^{pl} ($R^2 = 0.93$–1.00; Fig. 10c). For that reason, the different charge-balanced and

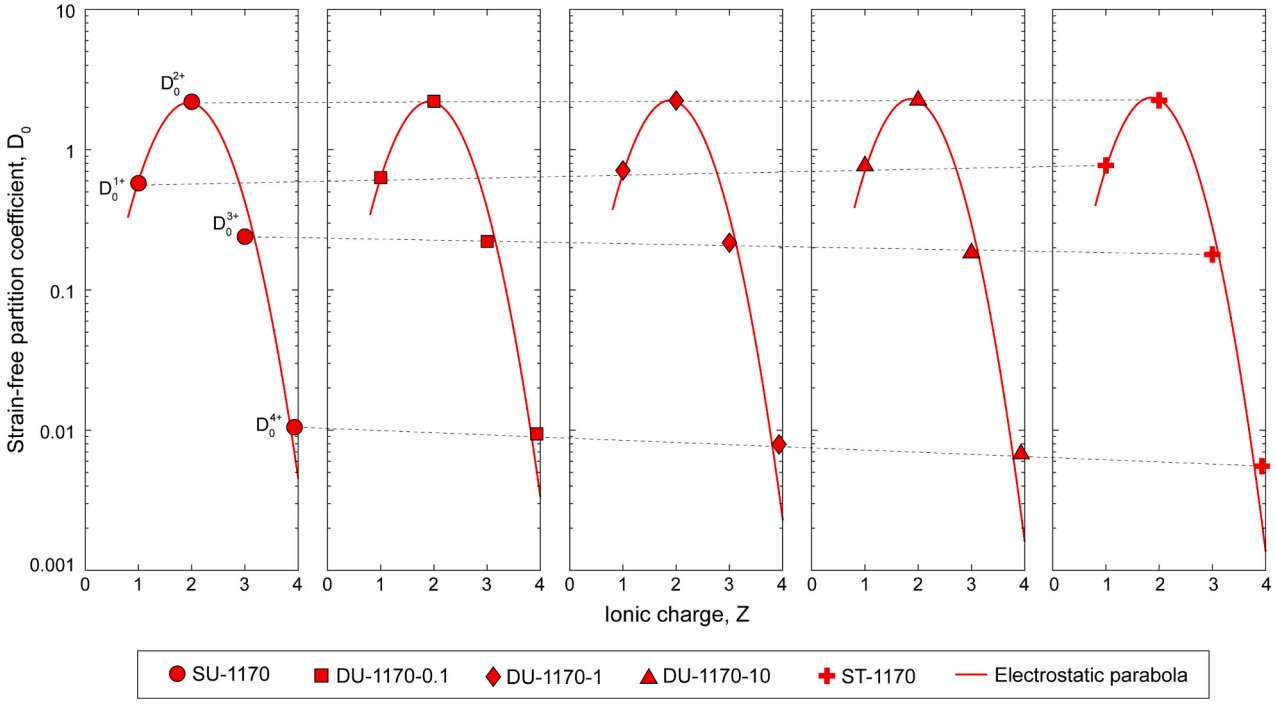

Fig. 9. Electrostatic parabolas for static and dynamic experiments, where the strain-free partition coefficients ${}^{M}D_0^{+1}$, ${}^{M}D_0^{+2}$, ${}^{M}D_0^{+3}$, and ${}^{M}D_0^{+4}$ are plotted against the charge Z of the corresponding cation. Parabolic fits are obtained using the electrostatic model of Wood and Blundy, 2001.

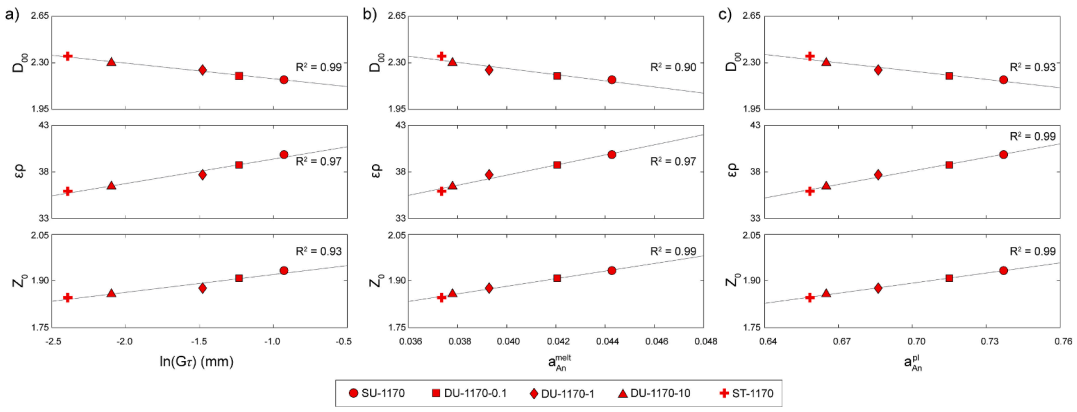

Fig. 10. The electrostatic parameters D_{00}, Z_0, and $\varepsilon\rho$ for static and dynamic experiments are compared with the textural attribute ln($G\tau$) (a), the activity of anorthite in plagioclase from models $M4_{1975}$ and $M1_{1992}$ of Kerrick and Darken (1975) and Holland and Powell (1992) (b), and the activity of anorthite in the melt from the model of Moschini et al. (2023) (c).

−imbalanced configurations produced by the accommodation of trace cations in the crystal lattice have a strong influence on the thermodynamic description of the partition coefficient. In particular, the topological variation observed for the electrostatic parabolas carries an energy penalty that is associated with plagioclase growth kinetics (Fig. 10a) and the concentration of major cations in the crystal structure (i.e., $a_{An}^{pl} = X_{An}^{pl}$ in Fig. 10c). At the same time, however, the leverage of electrostatic forces is mediated by the activity of anorthite in the melt (Fig. 10b) derived by the thermodynamic model of Moschini et al. (2023). Melt compositional effects account for a strong linearity between a_{An}^{melt} and a_{An}^{pl} ($R^2 = 0.99$), providing circumstantial evidence for a linear functional relation between melt and plagioclase activity compositions. Moreover, from simple mass balance considerations, the number of Ca-O-Si bonds in the melt is expected to increase with increasing a_{An}^{melt}, favoring the proportion of octahedral relative to tetrahedral sites in the melt structure. There is an increasing availability of non-bridging oxygens to form the cation-oxygen polyhedra in the silicate framework, especially for trace cations with a high charge density that can be roughly approximated to their Z_i/r_i ratio (cf. Di Stefano et al., 2019 and references therein). Consequently, D_0^{+3} and D_0^{+4} shift downward along the right-hand limb of the electrostatic parabola (Fig. 9) in response to the lower number of structural sites critically important to accommodating $^{M}i^{3+}$ and $^{M}i^{4+}$ in the melt adjacent to the crystal surface and supplying chemical nutrients to the newly formed crystalline layer of plagioclase.

The parameters $\varepsilon\rho$ and Z_0 cooperatively increase as the crystal growth rate increases (Fig. 10a), along with the activities of anorthite in both melt (Fig. 10b) and plagioclase (Fig. 10c). This mutual, linear variation suggests that the likelihood of charge-imbalanced configurations in M−sites of "wrong" −3 and −4 charges increases at the expense of the concentration of charge-balancing cations in adjacent structural sites (where the negative sign indicates the effective charge on an empty structural site; Wood and Blundy, 2001). The positive $\varepsilon\rho$-a_{An}^{pl} relation (Fig. 10c) is due to the great polarizability of Ca (Shannon, 1993) that causes an asymmetric charge distribution and repulsive forces between next-nearest neighbor cations in the crystal lattice. Coulombic iterations between ions change the enthalpy of mixing and are more facilitated in fast-growing, An^{pl}-rich crystals because of the smaller <Ca–O> interatomic distances in An^{pl} relative to <Na–O> in Ab^{pl} (Angel et al., 1988). According to this structural control, most of the charge excess into the coordination polyhedron is expected to increase because of the higher coulombic potential energy of fast-growing, An^{pl}-rich crystals. This effect shortens the coordinating cation–oxygen bond distances and enhances the proportion of charge-imbalanced configurations associated with heterovalent cation substitutions (Blundy and Wood, 2003a, 2003b; Wood and Blundy, 2003).

The dependence of Z_0 on a_{An}^{pl} (Fig. 10c) confirms that an electrostatic energy penalty must be paid for the entry of highly charged trace cations into the undisturbed matrix lattice. The larger the charge mismatch between Z_i and Z_0, the smaller is the magnitude of D_0^{+4} compared to D_0^{+3} (Mollo et al., 2020). Recalling that $\Delta G_{electrostatic} \approx -lnD_0RT$ from the original formulation of Wood and Blundy (2001), the average electrostatic energy calculated for D_0^{+4} $\left(\Delta G_{electrostatic\ ^{M}i^{4+}} = 58 \pm 3\,\mathrm{kJ\,mol^{-1}}\right)$ is effectively much higher than that obtained for D_0^{+3} $\left(\Delta G_{electrostatic\ ^{M}i^{3+}} = 19 \pm 2\,\mathrm{kJ\,mol^{-1}}\right)$. These two different energetic quantities indicate that heterovalent substitutions for $^{M}i^{3+}$ and $^{M}i^{4+}$ cause a surplus energy for the arrangement of ions at the lattice scale, so that excess charge dissipation across the lattice is governed by electrostatic compensation forces proportional to the charge difference between the substituent trace cation and the host major cation.

One final consideration ensuing from the comparison of lattice strain and electrostatic parameters is that the resistance of the lattice to local deformation E (Fig. 7b) and the region of electrostatic energy $\varepsilon\rho$ (Fig. 10a) are both correlated with ln($G\tau$). At the same time, the net positive optimum charge Z_0 resulting at the structural site (Fig. 10a) more readily attracts the coordinating oxygen anions in the polyhedron, thus lowering the optimum radius of the site r_0 (Fig. 7c). Using the standardized regression coefficient method, the overall influence exerted by ln($G\tau$) on E (17%), r_0 (16%), $\varepsilon\rho$ (17%), and Z_0 (18%) is equally distributed among the different parameters. This also denotes an axiomatic interdependence between strain and electrostatic properties, in consideration of the thermodynamic premise that partitioning energetics controlling trace cation substitutions in plagioclase are described by the complementary contributions of ΔG_{strain} and $\Delta G_{electrostatic}$. The basic tenet of these energetic terms is to settle the competition between charge-balanced and charge-imbalanced configurations taking place via incorporation of cations of very different size and charge, with consequent large enthalpic effects through distortion of the lattice and change in the coulombic forces. According to our thermodynamic parameterization, the statistical probability of encountering different structural arrangements by straining the lattice is counterbalanced by the prospect of finding charge mismatch sites for which electrostatic work of substitution must be done.

5. Conclusions

By interrogating the thermodynamics and kinetics of plagioclase crystallization from static (no physical perturbation) and dynamic (melt stirring) experiments, we document that the textural and compositional changes of crystals grown from a trachybasaltic melt are governed by

interface reaction kinetics resulting from the cooperative control of a small degree of effective undercooling, prolonged diffusive relaxation, and convective homogenization. The phenomenological implication of our experimental approach is the formation of near-homogeneous but compositionally distinct plagioclase populations as function of static and dynamic crystallization regimes, without the need to change the system temperature.

The partitioning of major, minor, and trace cations between plagioclase and melt is well constrained by a range of equilibrium partition coefficients estimated though a broad set of literature models, with the immediate repercussion that Onuma diagrams for isovalent groups of measured and modeled partition coefficients depict topologically equivalent parabolic patterns. The effectiveness of these models depends on their ability in describing the isothermal compositional dependence of partition coefficient on the mixing properties of plagioclase solution components, in order that the control of temperature on cation exchange reactions is adequately isolated and deconvolved from compositional effects.

The enthalpy change of cation substitutions is essentially dominated by the lattice strain energy in response to distortion of the lattice site, whilst the contribution of configurational entropy to partitioning reactions depends on activity-composition relations in both melt and crystal phases. On thermodynamic grounds, the energetics of cation partitioning are inextricably interrelated to the linearity between melt and plagioclase activity components, attesting that sluggish interface kinetics bring the system as close as possible to the ideality of plagioclase-melt relationships.

Since kinetics and thermodynamics are smoothly interconnected throughout the plagioclase growth process, different charge-balanced and −imbalanced configurations produced by the accommodation of trace cations into the coordination polyhedron of plagioclase can be thermodynamically rationalized in terms of lattice strain and electrostatic energetic quantities. In essence, there is a strong structural control governing the overall solution energy accompanying heterovalent substitutions, as most of the strain and charge excess is associated with the number of structural sites critically important to incorporate high charge density trace cations.

6. Data availability

Data are available through Mendeley Data at https://doi.org/10.17632/j8gngj9pxd.1.

CRediT authorship contribution statement

Silvio Mollo: Writing – review & editing, Writing – original draft, Methodology, Investigation, Formal analysis, Data curation, Conceptualization. **Fabrizio Di Fiore:** Writing – review & editing, Writing – original draft, Methodology, Investigation, Formal analysis, Data curation, Conceptualization. **Alice MacDonald:** Writing – review & editing, Methodology, Investigation, Formal analysis, Data curation, Conceptualization. **Teresa Ubide:** Writing – review & editing, Writing – original draft, Methodology, Investigation, Formal analysis, Data curation, Conceptualization. **Alessio Pontesilli:** Writing – review & editing, Writing – original draft, Methodology, Investigation, Formal analysis, Data curation, Conceptualization. **Gabriele Giuliani:** Writing – review & editing, Methodology, Formal analysis, Data curation. **Alessandro Vona:** Writing – original draft, Methodology, Formal analysis. **Claudia Romano:** Methodology, Formal analysis. **Piergiorgio Scarlato:** Methodology, Formal analysis.

Declaration of competing interest

The authors declare that they have no known competing financial interests or personal relationships that could have appeared to influence the work reported in this paper.

Acknowledgments

Part of this work was supported by MUR-PRIN 2022 PROVES Project (Grant #2022N4FBAA) and Sapienza University of Rome Research Project 2023 (Grant #RG123188A5C103FB) to SM, MUR-PNRR MEET Project (Grant #D53C22001400005) to FDF, AP and PS, and an Australian Research Council Discovery Project (ARC DP200101566) to TU. This paper benefited from thoughtful and constructive reviews by Yan Liang and an anonymous reviewer. Yuan Li and Jeffrey Catalano are also acknowledged for their editorial guidance, which was very greatly appreciated.

Appendix A. Supplementary material

Chemical analyses, textural data and partition coefficients for *SU-1170*, *DU-1170–0.1–1-10*, and *ST-1170* are comparatively provided as part of the Supplementary Material, together with the thermodynamic treatment relating the partition coefficients to melt activity products. Supplementary material to this article can be found online at https://doi.org/10.1016/j.gca.2024.09.006.

References

Aigner-Torres, M., Blundy, J., Ulmer, P., Pettke, T., 2007. Laser Ablation ICPMS study of trace element partitioning between plagioclase and basaltic melts: an experimental approach. Contrib. to Mineral. Petrol. 153, 647–667.
Angel, R.J., Hazen, R.M., McCormick, T.C., Prewitt, C.T., Smyth, J.R., 1988. Comparative compressibility of end-member feldspars. Phys. Chem. Miner. 15, 313–318.
Bédard, J.H., 2006. Trace element partitioning in plagioclase feldspar. Geochim. Cosmochim. Acta 70, 3717–3742.
Bédard, J.H., 2023. Trace element partitioning coefficients between terrestrial silicate melts and plagioclase feldspar: Improved and simplified parameters. Geochim. Cosmochim. Acta 350, 69–86.
Bindeman, I.N., Davis, A.M., 2000. Trace element partitioning between plagioclase and melt: investigation of dopant influence on partition behavior. Geochim. Cosmochim. Acta 64, 2863–2878.
Bindeman, I.N., Davis, A.M., Drake, M.J., 1998. Ion microprobe study of plagioclase-basalt partition experiments at natural concentration levels of trace elements. Geochim. Cosmochim. Acta 62, 1175–1193.
Blundy, J., Cashman, K., 2008. Petrologic reconstruction of magmatic system variables and processes. Rev. Mineral. Geochem. 69, 179–239.
Blundy, J.D., Wood, B.J., 1991. Crystal-chemical controls on the partitioning of Sr and Ba between plagioclase feldspar, silicate melts, and hydrothermal solutions. Geochim. Cosmochim. Acta 55, 193–209.
Blundy, J., Wood, B., 1994. Prediction of crystal-melt partition coefficients from elastic moduli. Nature 372, 452–454.
Blundy, J.D., Wood, B.J., Davies, A., 1996. Thermodynamics of rare earth element partitioning between clinopyroxene and melt in the system CaO-MgO-Al2O3-SiO2. Geochim. Cosmochim. Acta 60, 359–364.
Blundy, J., Wood, B., 2003a. Partitioning of trace elements between crystals and melts. Earth Planet. Sci. Lett. 210, 383–397.
Blundy, J., Wood, B., 2003b. Mineral-melt partitioning of uranium, thorium and their daughters. Uranium-Series Geochemistry 52, 59–123.
Cashman, K.V., 1990. Textural constraints on the kinetics of crystallization of igneous rocks. In: Nicholls, J., Russell, J.K. (Eds.), Modern Methods of Igneous Petrology: Understanding Magmatic Processes. Mineralogical Society of America, Reviews in Mineralogy 24, 259-314.
de Vries, J., van den Berg, A., van Westrenen, W., 2012. Formation and evolution of a lunar core from ilmenite-rich magma ocean cumulates. Earth Planet. Sci. Lett. 292, 139–147.
Di Fiore, F., Mollo, S., Vona, A., MacDonald, A., Ubide, T., Nazzari, M., Romano, C., Scarlato, P., 2021a. Kinetic partitioning of major and trace cations between clinopyroxene and phonotephritic melt under convective stirring conditions: New insights into clinopyroxene sector zoning and concentric zoning. Chem. Geol. 584, 120531.
Di Fiore, F., Vona, A., Kolzenburg, S., Mollo, S., Romano, C., 2021b. An extended rheological map of Pāhoehoe—'A'ā Transition. J. Geophys. Res. Solid Earth 126, 1–23.
Di Fiore, F., Vona, A., Costa, A., Mollo, S., Romano, C., 2022. Quantifying the influence of cooling and shear rate on the disequilibrium rheology of a trachybasaltic melt from Mt. Etna. Earth Planet. Sci. Lett. 594, 117725.
Di Fiore, F., Vona, A., Mollo, S., Nazzari, M., Giordano, G., Romano, C., 2023. Experimental insights on the shear-induced crystallization of a phonotephrite magma. Chem. Geol. 637, 121682.
Di Fiore, F., Vona, A., Di Genova, D., Pontesilli, A., Calabrò, L., Mollo, S., Taddeucci, J., Romano, C., Scarlato, P., 2024. Magma titanium and iron contents dictate crystallization timescales and rheological behaviour in basaltic volcanic systems. Commun. Earth Environ. 5, 283.

Di Stefano, F., Mollo, S., Blundy, J., Scarlato, P., Nazzari, M., Bachmann, O., 2019. The effect of CaO on the partitioning behavior of REE, Y and Sc between olivine and melt: Implications for basalt-carbonate interaction processes. Lithos 326–327, 327–340.
Di Stefano, F., Mollo, S., Ubide, T., Petrone, C.M., Caulfield, J., Scarlato, P., Nazzari, M., Andronico, D., Del Bello, E., 2020. Mush cannibalism and disruption recorded by clinopyroxene phenocrysts at Stromboli volcano: new insights from recent 2003–2017 activity. Lithos 360–361, 105440.
Dohmen, R., Blundy, J., 2014. A predictive thermodynamic model for element partitioning between plagioclase and melt as a function of pressure, temperature and composition. Am. J. Sci. 314, 1319–1372.
Drake, M.J., Weill, D.F., 1975. Partition of Sr, Ba, Ca, Y, Eu2+, Eu3+, and other REE between plagioclase feldspar and magmatic liquid: an experimental study. Geochim. Cosmochim. Acta 39, 689–712.
Forni, F., Petricca, E., Bachmann, O., Mollo, S., De Astis, G., Piochi, M., 2018. The role of magma mixing/mingling and cumulate melting in the Neapolitan Yellow Tuff caldera- forming eruption (Campi Flegrei, Southern Italy). Contrib. to Mineral. Petrol. 173, 45.
Gaetani, G.A., 2004. The influence of melt structure on trace element partitioning near the peridotite solidus. Contrib. to Mineral. Petrol. 147, 511–527.
Higgins, M.D., 2000. Measurement of crystal size distributions. Am. Mineral. 85, 1105–1116.
Higgins, M.D., 2006. Quantitative textural measurements in igneous and metamorphic petrology. Cambridge University Press, Cambridge.
Holland, T., Powell, R., 1992. Plagioclase feldspars: activity-composition relations based upon Darken's quadratic formalism and Landau theory. Am. Mineral. 77, 53–61.
Humphreys, M.C.S., Edmonds, M., Klöcking, M.S., 2016. The validity of plagioclase-melt geothermometry for degassing-driven magma crystallization. Am. Mineral. 101, 769–779.
Huppert, H.E., Sparks, R.S.J., 1980. The fluid-dynamics of a basaltic magma chamber replenished by influx of hot, dense ultrabasic magma. Contrib. Mineral. Petrol. 75, 279–289.
Iezzi, G., Mollo, S., Shahini, E., Cavallo, A., Scarlato, P., 2014. The cooling kinetics of plagioclase feldspar as revealed by electron-microprobe mapping. Am. Mineral. 99, 898–907.
Kempster, C.J.E., Megaw, H.D., Radoslovich, E.W., 1962. The structure of anorthite, $CaAl_2Si_2O_8$. I. Structure analysis. Acta Crystallogr. 15, 1005–1017.
Kennedy, A.K., Lofgren, G.E., Wasserburg, G.J., 1993. An experimental study of trace element partitioning between olivine, orthopyroxene and melt in chondrules: equilibrium values and kinetic effects. Earth Planet. Sci. Lett. 115, 177–195.
Kerrick, D.M., Darken, L.S., 1975. Statistical thermodynamic models for ideal oxide and silicate solid solutions, with application to plagioclase. Geochim. Cosmochim. Acta 39, 1431–1442.
Kneip, H.-J., Liebau, F., 1994. Feldspars with trivalent non-tetrahedral cations: experimental studies in the system $NaAlSi_3O_8$-$CaAl_2Si_2O_8$-$LaAl_3SiO_8$. Eur. J. Mineral. 6, 87–98.
Lang, S., Mollo, S., Lyderic, F., Misiti, V., Nazzari, M., 2021. Kinetic partitioning of major- minor cations between olivine and Hawaiian tholeiitic basalt under variable undercooling and cooling rate conditions. Chem. Geol. 584, 120485.
Lang, S., Mollo, S., Lyderic, F., Misiti, V., Nazzari, M., 2022. Partitioning of Ti, Al, P, and Cr between olivine and a tholeiitic basaltic melt: Insights on olivine zoning patterns and cation substitution reactions under variable cooling rate conditions. Chem. Geol. 601, 120870.
Lanzafame, G., Iezzi, G., Mancini, L., Lezzi, F., Mollo, S., Ferlito, C., 2017. Solidification and Turbulence (Non-laminar) during magma ascent: Insights from 2D and 3D analyses of bubbles and minerals in an Etnean dyke. J. Petrol. 58, 1511–1534.
Lasaga, A.C., 1998. Kinetic Theory in the Earth Sciences. Princeton University Press, Princeton.
Lofgren, G.E., Huss, G.R., Wasserburg, G.J., 2006. An experimental study of trace-element partitioning between Ti-Al-clinopyroxene and melt: equilibrium and kinetic effects including sector zoning. Am. Mineral. 91, 1596–1606.
Longhi, J., Walker, D., Hays, J.F., 1976. Fe and Mg in Plagioclase. Proc. Lunar Sci. Conf. 7, 1281–1300.
MacDonald, A., Ubide, T., Mollo, S., Masotta, M., Pontesilli, A., 2022. Trace element partitioning in zoned clinopyroxene as a proxy for undercooling: Experimental constraints from trachybasaltic magmas. Geochim. Cosmochim. Acta 336, 249–268.
Marsh, B.D., 1988. Crystal size distribution (CSD) in rocks and the kinetics and dynamics of crystallization – I. Theory. Contrib. to Mineral. Petrol. 99, 277–291.
Miller, S.A., Asimow, P.D., Burnett, D.S., 2006. Determination of melt influence on divalent element partitioning between anorthite and CMAS melts. Geochim. Cosmochim. Acta 70, 4258–4274.
Mollo, S., Hammer, J.E., 2017. Dynamic crystallization in magmas. In Mineral reaction kinetics: Microstructures, textures, chemical and isotopic signatures Mineralogical Society of Great Britain & Ireland, pp. 378–418.
Mollo, S., Putirka, K., Iezzi, G., Del Gaudio, P., Scarlato, P., 2011. Plagioclase-melt (dis) equilibrium due to cooling dynamics: Implications for thermometry, barometry and hygrometry. Lithos 125, 221–235.
Mollo, S., Misiti, V., Scarlato, P., Soligo, M., 2012. The role of cooling rate in the origin of high temperature phases at the chilled margin of magmatic intrusions. Chem. Geol. 322–323, 28–46.
Mollo, S., Blundy, J.D., Iezzi, G., Scarlato, P., Langone, A., 2013. The partitioning of trace elements between clinopyroxene and trachybasaltic melt during rapid cooling and crystal growth. Contrib. to Mineral. Petrol. 166, 1633–1654.
Mollo, S., Blundy, J., Scarlato, P., De Cristofaro, S.P., Tecchiato, V., Di Stefano, F., Vetere, F., Holtz, F., Bachmann, O., 2018. An integrated P-T-H2O-lattice strain model to quantify the role of clinopyroxene fractionation on REE+Y and HFSE patterns of mafic alkaline magmas: Application to eruptions at Mt. Etna. Earth-Science Rev. 185, 32–56.
Mollo, S., Blundy, J., Scarlato, P., Vetere, F., Holtz, F., Bachmann, O., Gaeta, M., 2020. A review of the lattice strain and electrostatic effects on trace element partitioning between clinopyroxene and melt: Applications to magmatic systems saturated with Tschermak-rich clinopyroxenes. Earth-Science Rev. 210, 103351.
Mollo, S., Moschini, P., Ubide, T., MacDonald, A., Vetere, F., Nazzari, M., Misiti, V., Miyajima, N., Melai, C., Di Genova, D., Vona, A., Di Fiore, F., Romano, C., 2023. Kinetic partitioning of trace cations between zoned clinopyroxene and a variably cooled-decompressed alkali basalt: Thermodynamic considerations on lattice strain and electrostatic energies of substitution. Geochim. Cosmochim. Acta 361, 40–66.
Morgan, D.J., Jerram, D.A., 2006. On estimating crystal shape for crystal size distribution analysis. J. Volcanol. Geotherm. Res. 154, 1–7.
Moschini, P., Mollo, S., Gaeta, M., Fanara, S., Nazzari, M., Petrone, C.M., Scarlato, P., 2021. Parameterization of clinopyroxene growth kinetics via crystal size distribution (CSD) analysis: Insights into the temporal scales of magma dynamics at Mt. Etna Volcano. Lithos 396–397, 106225.
Moschini, P., Mollo, S., Pontesilli, A., Nazzari, M., Petrone, C.M., Fanara, S., Vona, A., Gaeta, M., Romano, C., Scarlato, P., 2023. A review of plagioclase growth rate and compositional evolution in mafic alkaline magmas: guidelines for thermometry, hygrometry, and timescales of magma dynamics at Stromboli and Mt. Etna. Earth-Sci. Rev. 240, 104399.
Mutch, E.J.F., Maclennan, J., Madden-Nadeau, A.L., 2022. The dichotomous nature of Mg partitioning between plagioclase and melt: Implications for diffusion chronometry. Geochim. Cosmochim. Acta 339, 173–189.
Navrotsky, A., 1978. Thermodynamics of element partitioning: (1) Systematics of transition metals in crystalline and molten silicates and (2) Defect chemistry and "the Henry's law problem". Geochim. Cosmochim. Acta 42, 887–902.
Nielsen, R.L., Ustunisik, G., Weinsteiger, A.B., Tepley, F.J., Johnston, A.D., Kent, A.J., 2017. Trace element partitioning between plagioclase and melt: An investigation of the impact of experimental and analytical procedures. Geochem. Geophys. Geosyst. 18, 3359–3384.
O'Neill, H.S.C., Eggins, S.M., 2002. The effect of melt composition on trace element partitioning: an experimental investigation of the activity coefficients of FeO, NiO, CoO, MoO_2 and MoO_3 in silicate melts. Chem. Geol. 186, 151–181.
Onuma, N., Higuchi, H., Wakita, H., Nagasawa, H., 1968. Trace element partition between two pyroxenes and the host lava. Earth Planet. Sci. Lett. 5, 1–8.
Paton, C., Hellstrom, J., Paul, B., Woodhead, J., Hergt, J., 2011. Iolite: Freeware for the visualisation and processing of mass spectrometric data. J. Anal. Atomic Spectrometry 26, 2508–2518.
Peters, M.T., Shaffer, E.E., Burnett, D.S., Kim, S.S., 1995. Magnesium and titanium partitioning between anorthite and Type B CAI liquid: Dependence on oxygen fugacity and liquid composition. Geochim. Cosmochim. Acta 59, 2785–2796.
Pontesilli, A., Masotta, M., Nazzari, M., Mollo, S., Armienti, P., Scarlato, P., Brenna, M., 2019. Crystallization kinetics of clinopyroxene and titanomagnetite growing from a trachybasaltic melt: New insights from isothermal time-series experiments. Chem. Geol. 510, 113–129.
Putirka, K.D., 2005. Igneous thermometers and barometers based on plagioclase + liquid equilibria: Tests of some existing models and new calibrations. Am. Mineral. 90, 336–346.
Putirka, K., 2017. Geothermometry and Geobarometry. Encyclopedia of Geochemistry: A Comprehensive Reference Source on the Chemistry of the Earth. Springer International Publishing, Cham, pp. 1–19.
Ribbe, P.H., 1983. Aluminum-silicon order in feldspars; domain textures and diffraction patterns. In Mineralogical Society of America Reviews in Mineralogy 2, 2l–l.
Ryerson, F.J., Hess, P.C., 1978. Implications of liquid-liquid distribution coefficients to mineral-liquid partitioning. Geochim. Cosmochim. Acta 42, 921–932.
Schoneveld, L., O'Neill, H.S.C., 2019. The influence of melt composition on the partitioning of trace elements between anorthite and silicate melt. Contrib. to Mineral. Petrol. 174, 1–18.
Shannon, R.D., 1976. Revised effective ionic radii in oxides and fluorides. Acta Crystallogr. A 32, 751–757.
Shannon, R.D., 1993. Dielectric polarizabilities of ions in oxides and fluorides. J. Appl. Phys. 73, 348–366.
Sun, C., Graff, M., Liang, Y., 2017. Trace element partitioning between plagioclase and silicate melt: The importance of temperature and plagioclase composition, with implications for terrestrial and lunar magmatism. Geochim. Cosmochim. Acta 206, 273–295.
Tepley, F.J., Lundstrom, C.C., McDonough, W.F., Thompson, A., 2010. Trace element partitioning between high-An plagioclase and basaltic to basaltic andesite melt at 1 atmosphere pressure. Lithos 118, 82–94.
Ubide, T., Kamber, B.S., 2018. Volcanic crystals as time capsules of eruption history. Nat. Commun. 9, 1–12.
Vetere, F., Iezzi, G., Behrens, H., Holtz, F., Ventura, G., Misiti, V., Cavallo, A., Mollo, S., Dietrich, M., 2015. Glass forming ability and crystallisation behaviour of sub-alkaline silicate melts. Earth-Science Rev. 150, 25–44.
Watson, E.B., Müller, T., 2009. Non-equilibrium isotopic and elemental fractionation during diffusion-controlled crystal growth under static and dynamic conditions. Chem. Geol. 267, 111–124.
Wilke, M., Behrens, H., 1999. The dependence of the partitioning of iron and europium between plagioclase and hydrous tonalitic melt on oxygen fugacity. Contrib. to Mineral. Petrol. 137, 102–114.
Wood, B.J., 1976. Mixing properties of tschermakitic clinopyroxenes. Am. Mineral. 61, 599–602.
Wood, B.J., Blundy J.D., 2003. Trace element partitioning under crustal and uppermost mantle conditions: The influences of ionic radius, cation charge, pressure and

temperature. In: Carlson, R.W. (Ed.), The Mantle and Core. Treatise on Geochemistry. Vol. 2. Elsevier, Amsterdam, pp. 395–424.
Wood, B.J., Banno, S., 1973. Garnet-orthopyroxene and orthopyroxene-clinopyroxene relationships in simple and complex systems. Contrib. Mineral. Petrol. 42, 109–124.
Wood, B.J., Blundy, J.D., 2001. The effect of cation on crystal-melt partitioning of trace elements. Earth Planet. Sci. Lett. 188, 59–71.
Wood, B.J., Holland, T.J.B., Newton, R.C., Kleppa, O.J., 1980. Thermochemistry of jadeite—diopside pyroxenes. Geochim. Cosmochim. Acta 44, 1363–1371.
Worster, M.G., Huppert, H.E., Sparks, R.S.J., 1990. Convection and crystallization in magma cooled from above. Earth Planet. Sci. Lett. 101, 78–89.